

**SIMULATIONS AND MEASUREMENTS OF FUEL FILM USING REFRACTIVE
INDEX MATCHING METHOD**

by

FENGKUN WANG

THESIS

Submitted to the Graduate School

of Wayne State University,

Detroit, Michigan

in partial fulfillment for the requirements

for the degree of

MASTER OF SCIENCE

2014

MAJOR: MECHANICAL ENGINEERING

Approved by:

Advisor

Date

UMI Number: 1555607

All rights reserved

INFORMATION TO ALL USERS

The quality of this reproduction is dependent upon the quality of the copy submitted.

In the unlikely event that the author did not send a complete manuscript and there are missing pages, these will be noted. Also, if material had to be removed, a note will indicate the deletion.



UMI 1555607

Published by ProQuest LLC (2014). Copyright in the Dissertation held by the Author.

Microform Edition © ProQuest LLC.

All rights reserved. This work is protected against unauthorized copying under Title 17, United States Code



ProQuest LLC.
789 East Eisenhower Parkway
P.O. Box 1346
Ann Arbor, MI 48106 - 1346

DEDICATION

To my wife, Rui, and my daughter, Yingqi.

ACKNOWLEDGEMENTS

I want first to thank my advisor, Dr. Ming-Chia Lai, for his invaluable guidance and constant encouragement throughout the years of my study. He has been a source of inspiration and motivation for my research. Without his guidance and support, this research would not have been completed. I am also grateful to my other committee members, Dr. Marcis Jansons and Dr. Trilochan Singh, for their time in reviewing my thesis.

I would like to especially thank Dr. Xingbin Xie for his dedicated support, insightful comments and guidance. I offer my regards to the lab colleagues who worked together throughout the research, especially to Dr. Po-I Lee, Mr. Huijun Li, and Mr. Xiaoce Feng who assisted me with their knowledge and experience in this field of study.

Finally, I would like to thank my family for being supportive and patient throughout the years. I owe special thanks to my wife, Rui Guo, for her love and encouragement.

TABLE OF CONTENTS

DEDICATION.....	ii
ACKNOWLEDGEMENTS	iii
LIST OF TABLES.....	vi
LIST OF FIGURES.....	vii
CHAPTER 1 INTRODUCTION.....	1
1.1 Background.....	1
1.2 Scopes of Thesis Work and Thesis Outline.....	2
CHAPTER 2 Literature Review.....	4
2.1 RIM.....	4
2.2 CFD.....	6
CHAPTER 3 STUDY METHODOLOGY.....	9
3.1 Experimental Setup.....	9
3.1.1 Spray Visualization Setup	9
3.1.2 Spray Impingement and RIM Setup.....	11
3.1.3 Numerical Simulation Setup of Spray and Wall Impingement	20
CHAPTER 4 RESULTS AND DISCUSSIONS	24
4.1 Spray and Wall Impingement	24
4.2 Wall Impingement and RIM.....	29
4.2.1 Injection Angle Effect.....	29
4.2.2 Fuel Pressure Effect	35
4.2.3 Air Pressure Effect	37

4.2.4	Simulation Results of Wall film	42
CHAPTER 5	CONCLUSION.....	44
5.1	Summary of the Work	44
5.2	Recommendation and Future Work	44
REFERENCES	45
ABSTRACT	48
AUTOBIOGRAPHICAL STATEMENT	49

LIST OF TABLES

Table 3.1 Fuel properties at 1bar and 298K	11
Table 3.2 Specifications of tested injectors for spray	11
Table 4.1 Test conditions for spray vaporization.....	24
Table 4.2 Test matrix of wall film.....	29

LIST OF FIGURES

Figure 3.1 Experimental setup of Schlieren spray visualization: (a) schematic image, (b) photograph.	10
Figure 3.2 Experimental setup of RIM method: (a) schematic image, (b) photograph.	12
Figure 3.3 Spatial distribution of the scattering light intensity variation	15
Figure 3.4 2D distribution of the fluorescent light intensity	16
Figure 3.5 Fitting of the 1D fluorescent intensity using parabolic function.....	16
Figure 3.6 1D distribution of film thickness and intensity variation	17
Figure 3.7 Relation between film thickness and intensity variation.....	18
Figure 3.8 Curve fitting of the calibration	19
Figure 3.9 Image processing of the RIM images, (a) Raw image, (b) Background removed image, (c) Binary image, (d) Time filtered image, and (e) Time and space filtered image.	20
Figure 3.10 KH-RT breakup model.	21
Figure 3.11 Collision regimes of spray wall interaction used in Converge.....	22
Figure 3.12 Collision regimes of spray wall interaction used in Fluent	23
Figure 4.1 Schematic Figure (a) and apparatus photo (b) of injection rate meter.....	25
Figure 4.2 Injection rates under injection pressures of 70bar and 100bar.....	26
Figure 4.3 Experimental and CFD penetration of Case1(a), Case2(b), Case3(c) and Case4(d)	27
Figure 4.4 Spay Comparison between experimental and CFD results	28
Figure 4.5 Wall films with different injection angles under $T_{air}=50C$, $P_{air}=2bar$, $T_{fuel}=55C$, $P_{fuel}=100bar$, total area (a), total mass (b), average thickness (c)	30

Figure 4.6 Wall films with different injection angles under $T_{air}=50C$, $P_{air}=2bar$, $T_{fuel}=55C$, $P_{fuel}=70bar$, total area (a), total mass (b), average thickness (c)	31
Figure 4.7 Wall films with different injection angles under $T_{air}=50C$, $P_{air}=2bar$, $T_{fuel}=55C$, $P_{fuel}=140bar$, total area (a), total mass (b), average thickness (c)	32
Figure 4.8 Wall films with different injection angles under $T_{air}=50C$, $P_{air}=1bar$, $T_{fuel}=55C$, $P_{fuel}=70bar$, total area (a), total mass (b), average thickness (c)	33
Figure 4.9 Wall films with different injection angles under $T_{air}=75C$, $P_{air}=1bar$, $T_{fuel}=55C$, $P_{fuel}=70bar$, total area (a), total mass (b), average thickness (c)	34
Figure 4.10 Wall films with P_{fuel} under $T_{air}=50C$, $P_{air}=2bar$, $T_{fuel}=55C$, $\theta_{inj}=30^\circ$, total area (a), total mass (b), average thickness (c).....	36
Figure 4.11 Wall films with different P_{fuel} under $T_{air}=50C$, $P_{air}=2bar$, $T_{fuel}=55C$, $\theta_{inj}=60^\circ$, total area (a), total mass (b), average thickness (c)	37
Figure 4.12 Wall films with different P_{air} under $T_{air}=50C$, $T_{fuel}=55C$, $P_{fuel}=70bar$, $\theta_{inj}=30^\circ$, total area (a), total mass (b), average thickness (c)	38
Figure 4.13 Wall films with different P_{air} under $T_{air}=50C$, $T_{fuel}=55C$, $P_{fuel}=70bar$, $\theta_{inj}=60^\circ$, total area (a), total mass (b), average thickness (c)	39
Figure 4.14 Wall films with different T_{air} under $P_{air}=1bar$, $T_{fuel}=55C$, $P_{fuel}=70bar$, $\theta_{inj}=30^\circ$, total area (a), total mass (b), average thickness (c)	40
Figure 4.15 Wall films with different T_{air} under $P_{air}=1bar$, $T_{fuel}=55C$, $P_{fuel}=70bar$, $\theta_{inj}=60^\circ$, total area (a), total mass (b), average thickness (c)	41
Figure 4.16 Comparison between experimental and CFD results of wall film.....	42

CHAPTER 1 INTRODUCTION

1.1 Background

Nowadays, internal combustion engines (ICE) are widely used in transportation and individual mobility and contribute to air pollution and greenhouse gases, such as soot, nitrogen oxide (NO_x), carbon monoxide (CO) or carbon dioxide (CO₂). In the United States, 97.5% of transportation CO₂ emissions came from petroleum-derived fuels in 2010. Gasoline powered vehicles have been responsible for 63.8% of U.S. CO₂ emissions over the last twenty years. The majority of CO (61.8%) and NO_x (50.9%) emissions comes from transportation, especially from highway vehicles [1]. Concerning energy and environmental problems, critical standards of emission and fuel consumption for passenger vehicles have been proposed by governments all over the world, and the goals include increasing power output, improving fuel economy and decreasing pollutant emissions of ICE.

To achieve these goals, more and more new engine technologies, such as direct fuel injection (DI), turbocharge, and variable valve timing/actuation (VVT/VVA), have been used [2]. Among these engine technologies, DI is a promising technology for next generation ICE. Compared to a spark-ignition engine equipped with a port fuel injection (PFI) system, direct-injection spark-ignition (DISI) combustion has lower fuel consumption, faster transient response, more precise control of air-fuel ratio, and lower pollutant emission. The DI gasoline engine prevails in many vehicle manufacturing companies; for example, Ford announced that 90% of its global vehicles were equipped with DI gasoline engines in 2013 [3].

Although gasoline-direct injection engines have many advantages, the deposit (fuel film) of the injected liquid fuel on the liner or the piston top is a big issue, which is inevitable and the source of unburned hydrocarbons (UTC) and particle matter (PM) [4]. Therefore, the study of fuel film is critical for DI gasoline engines to improve their fuel efficiency and reduce emissions. Among the methods used to measure fuel film, the Refractive Index Matching (RIM) technique is reliable and can be easily applied to temporal and spatial quantitative measurements of fuel film under vaporizing conditions. In terms of simulation, multi-dimensional computational fluid dynamics (CFD) can provide a more detailed insight into fuel film, which can help to understand the problem better.

1.2 Scope of Thesis Work and Thesis Outline

The objective of this study is to characterize the fuel film spatially and temporally through both experimental and CFD modeling. The measurement of the wall film thickness and mass is carried out by experimentally using the RIM technique.

Chapter 2 reviews DI spray and spray wall interaction.

Chapter 3 addresses the study methodology. The research has been accomplished by RIM and 3D CFD simulation. The experimental setups for the spray visualization and fuel film measurement using RIM are first illustrated. Second, the computational models are demonstrated including mesh management, turbulence model; spray model, and liquid film model.

Chapter 4 first presents the experimental results for spray vaporization and fuel film measured using schlieren and RIM techniques. Simulation results are

demonstrated as well to compare the experimental data and investigate the spray and spray wall interaction in more detail.

Chapter 5 summarizes the work in this thesis and recommends future work for research based on the findings here.

CHAPTER 2 Literature Review

This chapter presents a literature review about published experimental and computational wall film research. The purpose of this review is to compare the advantages and disadvantages of different methods and to identify a path of improving the wall film research.

2.1 RIM

The RIM method can be used to measure the spatial and temporal thickness of the fuel film and was used by Drake et al. in 2002 [5]. The principle of the RIM method is based on the relationship between the film thickness and scattering light intensity that can be obtained from the digital picture. In 2003, Drake et al. measured the thickness, area and mass of the fuel film on the top of the piston in an optical access engine (OAE) [5]. Furthermore, they successfully correlated the fuel film with the emission with UTC and PM [6]. In the experiment, isooctane was used as fuel, and the calibration was carried out by dipping a drop of isooctane with a known volume on ground glass. It was assumed that the droplet would form a flat film after it fully spread on the glass; then, the average film thickness was calculated and correlated with the average scattering light intensity. However, there are two issues with this calibration. First, the shape of a free steady droplet is parabolic instead of flat. Second, the scattering light intensity will be saturated when the film thickness exceeds a certain value. Unfortunately, the authors did not evaluate the effects of the droplet shape and saturation of scattering light on the calibration results. The results would have been more reliable if the authors had taken into account these two factors. In 2007, Yang and Ghandhi measured the fuel film for a diesel injector

using the RIM method in a constant volume chamber with the ambient temperature up to 500K [7]. In their study, the peak thickness of the fuel film was 5 μm , which is a little higher than what Drake et al. obtained of 1 μm due to the different ambient conditions. Although the results obtained by Yang and Ghandhi were reproducible, the calibration had the same problem as that of Drake et al. Again, the droplet shape and saturation of scattering light were not taken into account, which resulted in the same experimental error.

In 2012, Zheng et al. used the RIM method to measure the film thickness of a gasoline injector in a constant volume chamber [8]. Different from the methods used by former researchers, a mixture of isooctane and dodecane was used for the calibration, in which a syringe (which can deliver the minimum volume of 0.1 μL and the liquid mixture of 10% by volume of dodecane and 90% by volume of isooctane) was used. The authors assumed that the isooctane would evaporate much more quickly than the dodecane after a drop of liquid mixture is dripped on the glass by the syringe, and the remaining liquid would be only dodecane when the changing rate of the liquid film area begins to slow down. Then, the volume and the area of the film at this time could be used to calculate the average film thickness and be further correlated with scattering intensity. However, the interaction between the dodecane and isooctane was ignored, which affected the calibration dramatically. Although isooctane easily evaporates, dodecane will dissolve some isooctane. The liquid left is not pure dodecane but the solvent of dodecane and isooctane, and the liquid volume should be larger than what is occupied by the pure dodecane. As a result, the calibration in this paper tends to underestimate the film thickness. To improve

the calibration, the actual volume of the liquid film should consist of the volume of the dodecane and the volume of the solved isooctane, which depends on the pressure, temperature and the properties of isooctane and dodecane. Another issue in this calibration is that the scattering light intensity spans from 0.6 to 0.9, which is only one third of the whole intensity range, 0-1, so it is not very convincing to use this data to extrapolate the whole function between the film thickness and the scattering light intensity. If the authors had changed the ratios between isooctane and the dodecane in the liquid mixture instead of only 1:9, they would have obtained more calibration points over a wider range of scattering intensity, and the calibration would have been more reliable.

From the aforementioned study of RIM, it is known that the precision of the calibration will affect the final result dramatically, and there is still more work to be done in the future. First, it is a better choice to keep the liquid used in the calibration the same as what is used in the experiments. Second, the droplet shape and the saturation of the scattering light must be taken into account in the calibration.

2.2 CFD

Multi-dimensional CFD offers a promising alternative to experiments due to its capability to offer much more detailed information on spray and wall film. Numerical methods are still a challenge today because the sub-models used to simulate the physical phenomena of spray and wall film are not sufficiently validated. Thus, more accurate models and experimental data are needed to improve the simulation [9]. The wall film thickness generated diesel spray has been simulated by considering and evaluating the heat transfer between the temperature-controlled wall and

impinging spray [10], but conjugate heat transfer and spray cooling effect were not taken into account. The effects of injection pressure and wall inclination angle on the multi-hole GDI spray were investigated experimentally and numerically [11], but the wall film generated by the spray was not investigated. In 2012, a detailed simulation of fuel film was conducted by Zheng et al. [8]. In the CFD models, the Kelvin-Helmholtz/Rayleigh-Taylor (KH-RT) breakup model was used to simulate the spray. Very good agreements between the experiments and simulation of the film shape were obtained in Zheng et al.'s work. The numerical penetrations of the spray also matched well with the experimental results. However, the film thickness in the simulation was larger than that of the experiments, and this may be due to underestimating the film thickness in the experiments as mentioned above. The authors also claimed that the liquid film evaporated more quickly in the simulation, but they did not give a detailed explanation. The reason may be that the conjugate heat transfer model is missing in the simulation. In the experiments, the temperature of the wall will decrease while the liquid film is evaporating after the spray hits the wall; then the evaporation rate of the liquid film will decrease due to the lower wall temperature. However, in the simulation, the temperature of the wall was set to a constant value, which will lead to a faster evaporating rate of the liquid film. Therefore, a conjugate heat transfer model should be taken into account if the authors wanted to get more reasonable results.

In summary, RIM is a powerful technique in the measurement of fuel film because it can measure the local film thickness spatially and temporally and provide much more detailed information about fuel film. However, the precision of the

measurement using RIM will be dramatically affected by the calibration. The shape of the free droplet and the saturation of scattering light play a great roll in the calibration, but they have been unfortunately ignored by previous researchers. In terms of simulation, conjugate heat transfer is essential to the evaporation of fuel film, state of the art CFD models should be employed to simulate the fuel film better. Thus, more work is necessary on both experiments and CFD to improve the study of fuel film. In this work, a more careful calibration will be first carried out based on the droplet shape and saturation of the scattering light; then, CFD simulation will be performed using the conjugate heat transfer model.

CHAPTER 3 STUDY METHODOLOGY

In this chapter, the optical diagnostics and numerical methods in spray visualization and wall film measurement will be discussed.

3.1 Experimental Setup

In this section, the instrument setup and data processing method in spray visualization and the RIM technique are presented.

3.1.1 Spray Visualization Setup

Spray and wall impingement visualization experiments are conducted in a spray constant volume vessel chamber without charge motion, which is suitable for detail study of the spray and vaporization, wall impingement and wall film.

The schlieren visualization technique was adopted to characterize the sprays of a vertically mounted single-hole nozzle injector.

The experiment apparatus and optical setup for the Schlieren spray visualization method is presented in Fig. 3.1. The cylindrical chamber is made of carbon steel with the inner diameter and length of $\Phi 150 \text{ mm} \times 180 \text{ mm}$. The light from a projection lamp forms parallel rays after travelling through the tiny pinhole and the expansion lens. The collimated light then passes through the chamber and is focused by another lens. A knife edge is placed on this focal point to block half of the refracted light. Finally, the beam is collected by a high speed digital camera with a resolution of 512×512 pixels and synchronized with the injector by a signal generator.

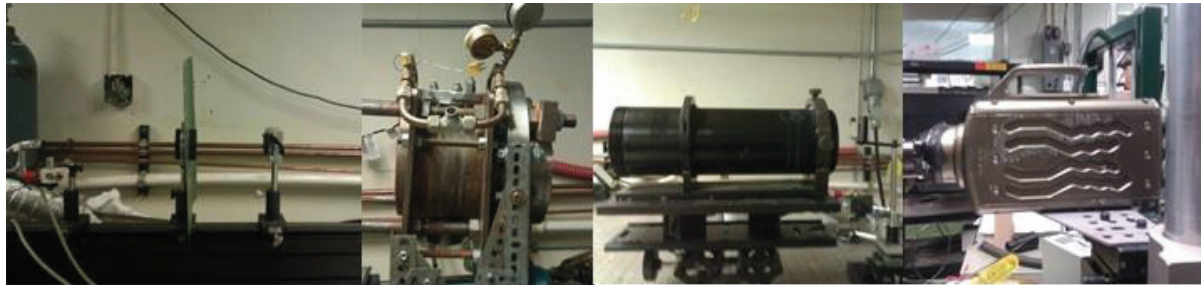
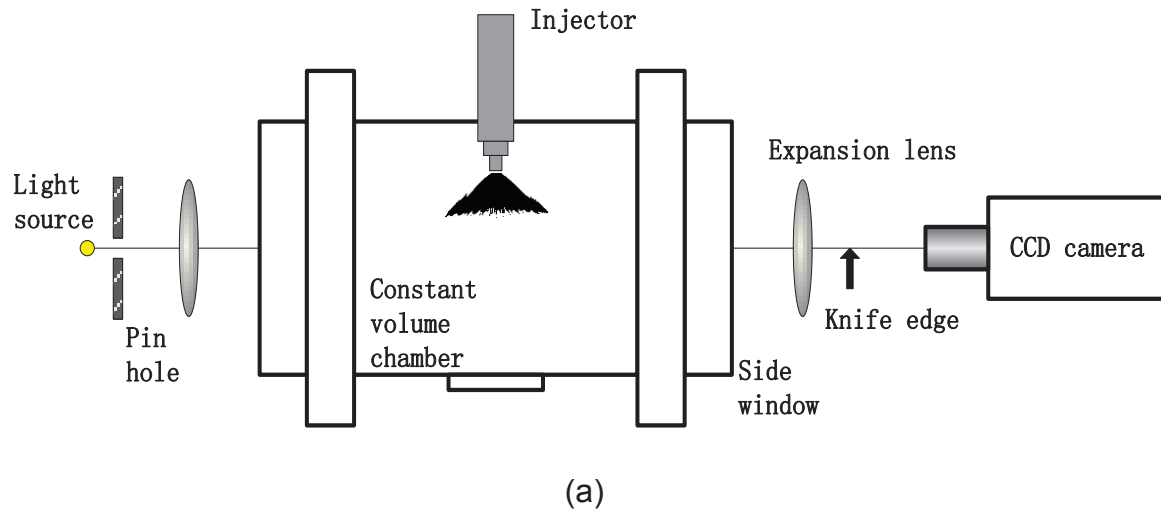


Figure 3.1 Experimental setup of Schlieren spray visualization: (a) schematic image, (b) photograph.

The spray visualization experiments were carried out to image the spray structures under typical DI engine fuel injection conditions. 100% pure ethanol (E100) was used in the tests, and the main properties of E100 are shown in Table 3.1. The specifications of GDI injector A, which was designed for research, are listed in Table 3.2. The spray images were taken at 1 ms after start of injection (ASOI), unless otherwise specified.

Table 3.1 Fuel properties at 1bar and 298K

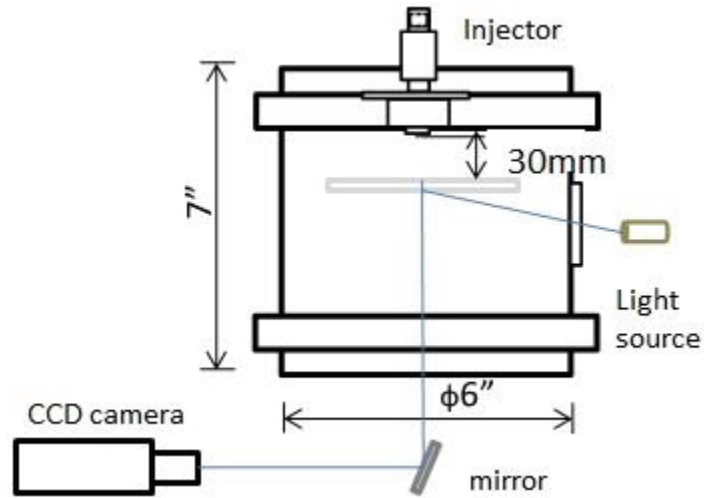
	Ethanol	Gasoline
Density [kg/m ³]	785	737
Viscosity [10 ⁻⁶ m ² /s]	1.52	0.46
Surface Tension [10 ³ N/m]	21.9	22
Latent Heat of Vaporization [kJ/kg]	865	380-500

Table 3.2 Specifications of tested injectors for spray

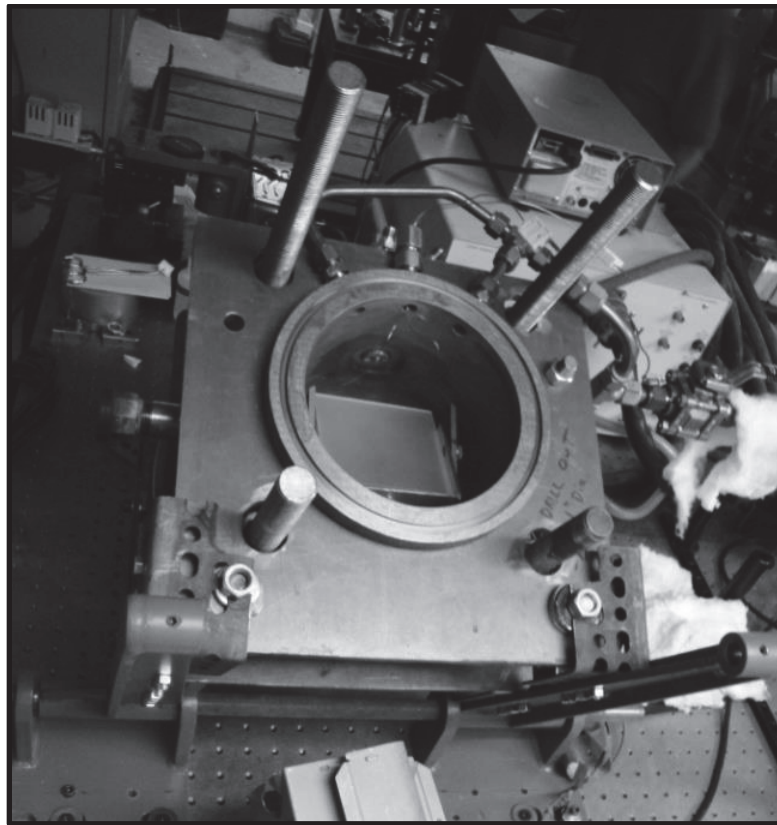
	Single-holes injector A
Nozzle diameter (mm)	0.22
Nozzle length (mm)	0.31
Averaged L/D ratio	1.41
Number of holes	6
Static mass flow with ethanol (g/s)	2.55

3.1.2 RIM Setup

The RIM tests were carried out for the same injector. The injection pressure varied from 70bar to 140bar, which can be changed by regulating the nitrogen pressure at the gas tank. Pure ethanol was used in the calibration and tests of liquid film thickness with the RIM technique.



(a)



(b)

Figure 3.2 Experimental setup of RIM method: (a) schematic image, (b) photograph.

The experiment setup for calibration and wall film measurements using RIM is displayed in Fig. 3.2. The single-hole GDI injector A was vertically mounted on the top of the chamber. A 140mm diameter 50mm thick quartz windows was mounted on the bottom of the pressurized chamber, and one 60mm diameter 20mm thick quartz window was on the side. The pressurized chamber can be heated up to 250°C by a circulation air heater and pressured up to 4bar. A flat optical ground glass diffuser (N-BK7, Thorlabs), 100mm × 100mm × 2mm, was placed in the pressurized chamber horizontally. Various grit polishes on the diffuser were tested, but the results presented in this paper were obtained using the 220 grit polish, which showed the best sensitivity to the range of film thickness of interest. Lighting was provided by a continuous projection lamp from the side window with an incident angle of about 10°. The images were captured with a high speed digital CCD camera through a mirror placed directly beneath the ground glass and outside the spray chamber.

The RIM technique measures the spatial distribution of the fuel film thickness, from which the adhered puddle mass can be calculated. In this method, the difference in the index of refraction between the impinging surface and air results in the scattering of light off the roughened surface, which is modified by the presence of a liquid that closely matches the index of refraction of the impingement window. Drake et al. [5][6], showed that the relation between the fuel film thickness and the variation of intensity in the scattered light. The reflection variation (reduction) through the window was written as:

$$\Delta I(x, y) = 1 - \frac{I_{wet}(x, y)}{I_{dry}(x, y)} \quad \text{Equation 3.1}$$

where I_{dry} is the intensity of the scattered light in reference image at the location of (x, y) and I_{wet} is the intensity with liquid deposit.

After the calibration procedure was performed, a function f can be built between the liquid film thicknesses $h(x, y)$ and the reflection variation in the scattered light: ΔI :

$$h(x, y) = f(\Delta I) \quad \text{Equation 3.2}$$

The calibration was carried out at ambient condition. By an AccuPet Pro precision digital syringe, a known volume liquid was dropped on the ground glass. The minimum volume that can be delivered is $0.1\mu\text{L}$. The averaged reference dry image was obtained before the liquid was deposited on the window. The liquid droplet rapidly expands after it deposits on the roughened window surface. The total deposited wet area increases firstly, then decrease due to the evaporation. A MATLAB program was used to count the number of black pixels to obtain the area size. To calculate the volume of the droplet at different times, it is assumed that the evaporation rate, the evaporated liquid per area and per time, is constant, which can be obtained from the integration of the whole process.

$$V_0 = \int_0^{t_{end}} C_E A dt \quad \text{Equation 3.3}$$

where V_0 is the initial volume, t is time, t_{end} is the time of the whole process, A is the transient wetting area at each time point, and C_E is the evaporation constant. With evaporation constant, the volume of the droplet at any time can be calculated using the following equation:

$$V = V_0 - \int_0^t C_E A dt \quad \text{Equation 3.4}$$

An important factor that needs to be concerned in the calibration is the saturation of the scattering light, which means that the scattering light intensity will not change after the film thickness is beyond a certain value as shown in Figure 3.3.

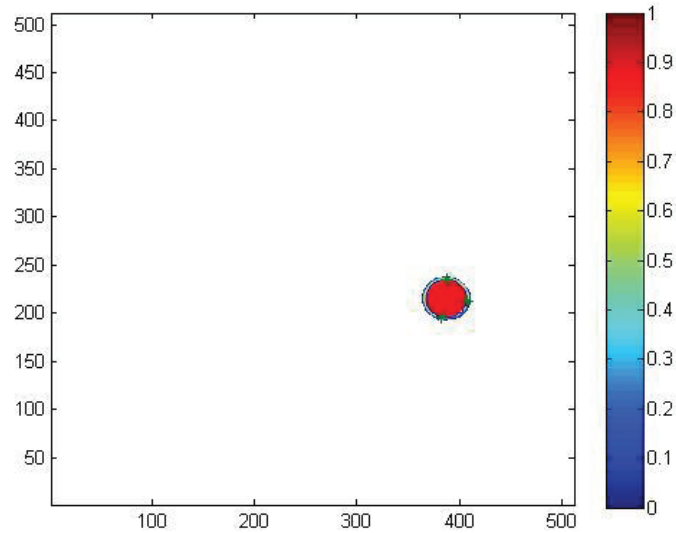


Figure 3.3 Spatial distribution of the scattering light intensity variation

To eliminate the effect of the saturation of the scattering light, the shape of the droplet was treated as a parabolic profile [12] and verified using the laser fluorescent method, in which a solution of a fluorescent dye (Rhodamine B) in ethanol was used. The intensity of active fluorescent light is proportional to the amount of the dye, which is a linear function of the local film thickness. Thus, the fluorescent light intensity can represent the film thickness. The 2D distribution of the fluorescent light intensity is shown in Figure 3.4, and the 1D light intensity along the diameter and fitting is shown in Figure 3.5. Here, the 1D light intensity is the average of the 2D result along the diameter direction. In Figure 3.5, it can be seen that the

profile of the droplet is very close to a parabolic curve. Thus, it is reasonable to treat the droplet shape as parabolic in the calibration.

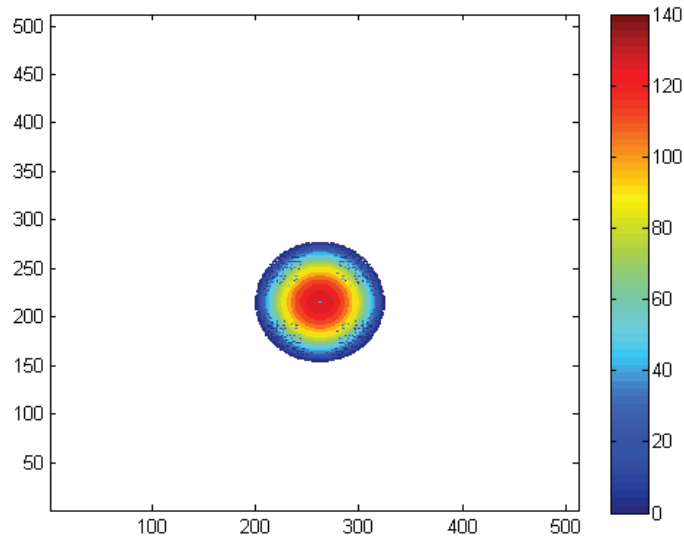


Figure 3.4 2D distribution of the fluorescent light intensity

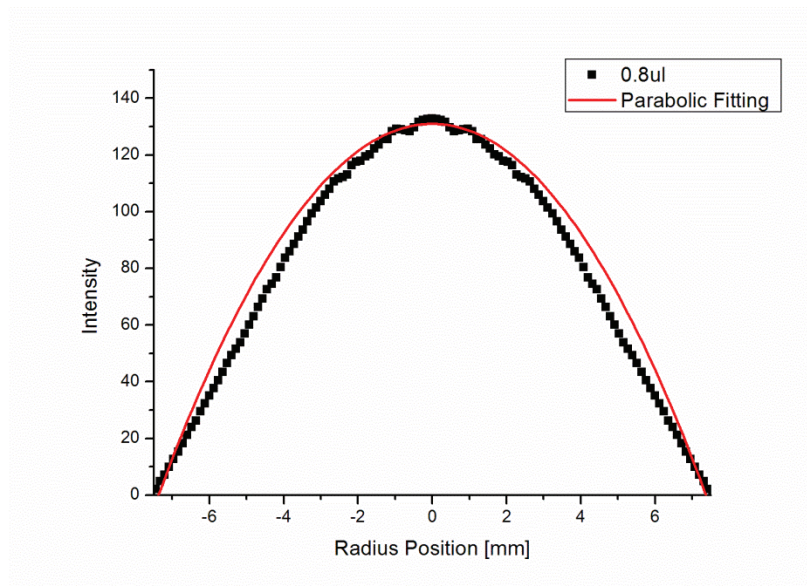


Figure 3.5 Fitting of the 1D fluorescent intensity using a parabolic function

In the calibration, the instantaneous wetting area was obtained from the digital picture, and the corresponding droplet volume was calculated using equations 3.3 and 3.4. Based on the instant area, volume, and the parabolic profile, the 1D film thickness can be obtained. The 1D distribution of film thickness and scattering light intensity variation are shown in Figure 3.6, in which the red symbols represent the film thickness, and the black spots are the intensity variation of the scattering light. It can be seen that the intensity variation does not change after the film is thicker than $15\mu\text{m}$. Thus, only the data near the edge of the liquid film can be used for further calibration.

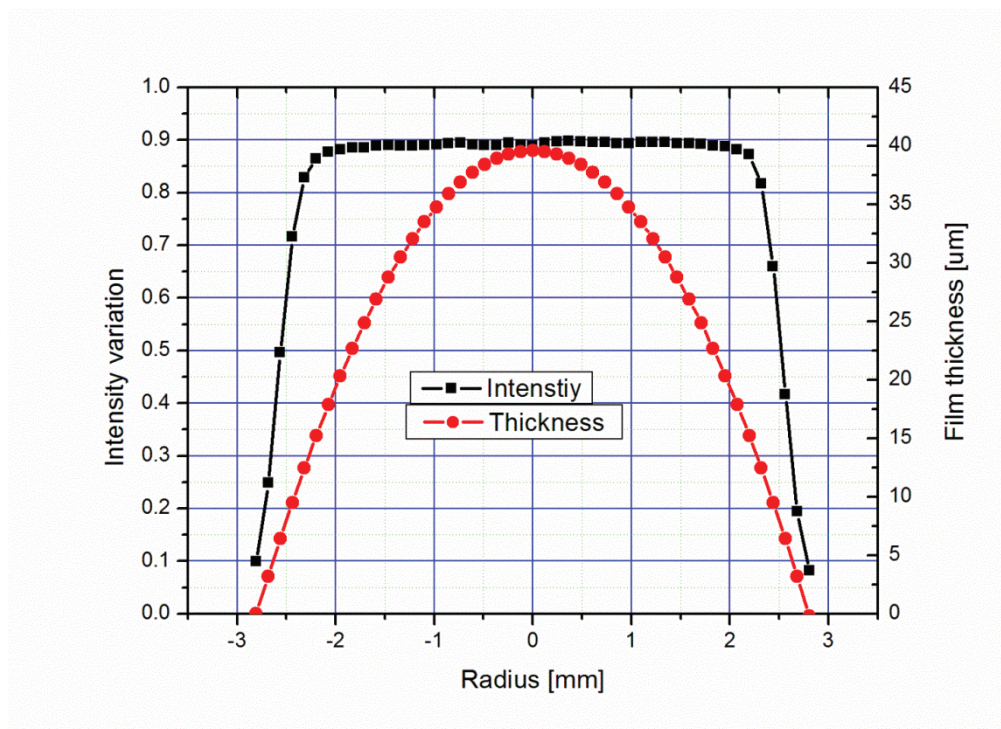


Figure 3.6 1D distribution of film thickness and intensity variation

The calibration was repeated using liquid droplets with different volumes, and the relationship between the film thickness and intensity variation is shown in Figure 3.7. From Figure 3.7, it can be seen that there is good coherence between different

calibrations using different volumes of droplets. When intensity variation is larger than 0.8, the film thickness increases dramatically, which means the scattering light intensity is saturated and changes with increasing film thickness. Thus, only the data with intensity variations less than 0.8 can be used for further curve fitting, and the fitting result is shown in Figure 3.8.

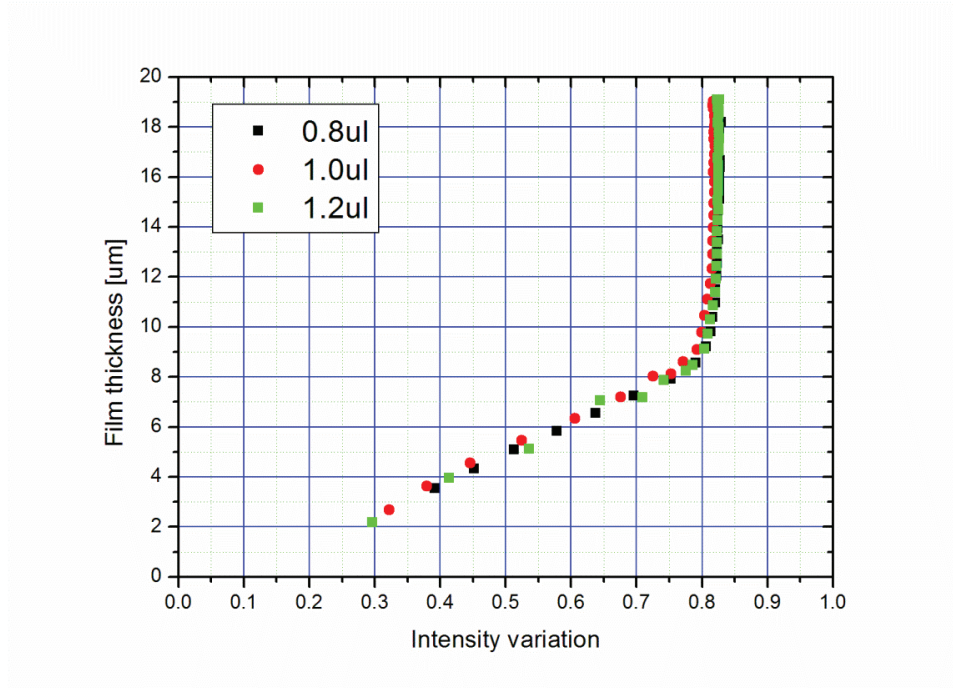


Figure 3.7 Relation between film thickness and intensity variation

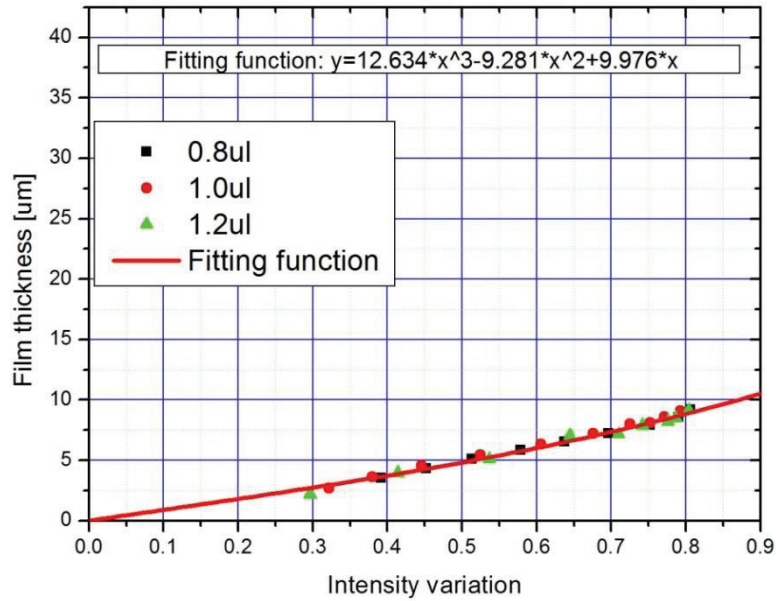


Figure 3.8 Curve fitting of the calibration

After the calibration procedure, the single-hole injector was mounted vertically on the top of the chamber as shown in Fig. 3.2. Fuel was injected on the rough flat glass at various ambient conditions and injection conditions and with the same optical setup.

The processing of RIM experiment images is shown in Fig. 3.9. First, the averaged reference image was subtracted from the wetting images to calculate the reduction in scattered light ΔI . This was then converted to a binary image that was used to obtain the instantaneous area of the deposit film. To eliminate the noise on the background image, time and space filtering were carried out to improve the image quality. For the time filter, a fixed-point filter is used to average a sequence of images with window size of 10. For the space filter, a mean filter is adapted to 3x3 blocks. Fig. 3.9d and Fig. 3.9e show the filled contour of images that applied the

time filter and space filters, respectively. A color coded image is used to accentuate the intensity, with the red region representing high intensity and blue region representing low intensity.

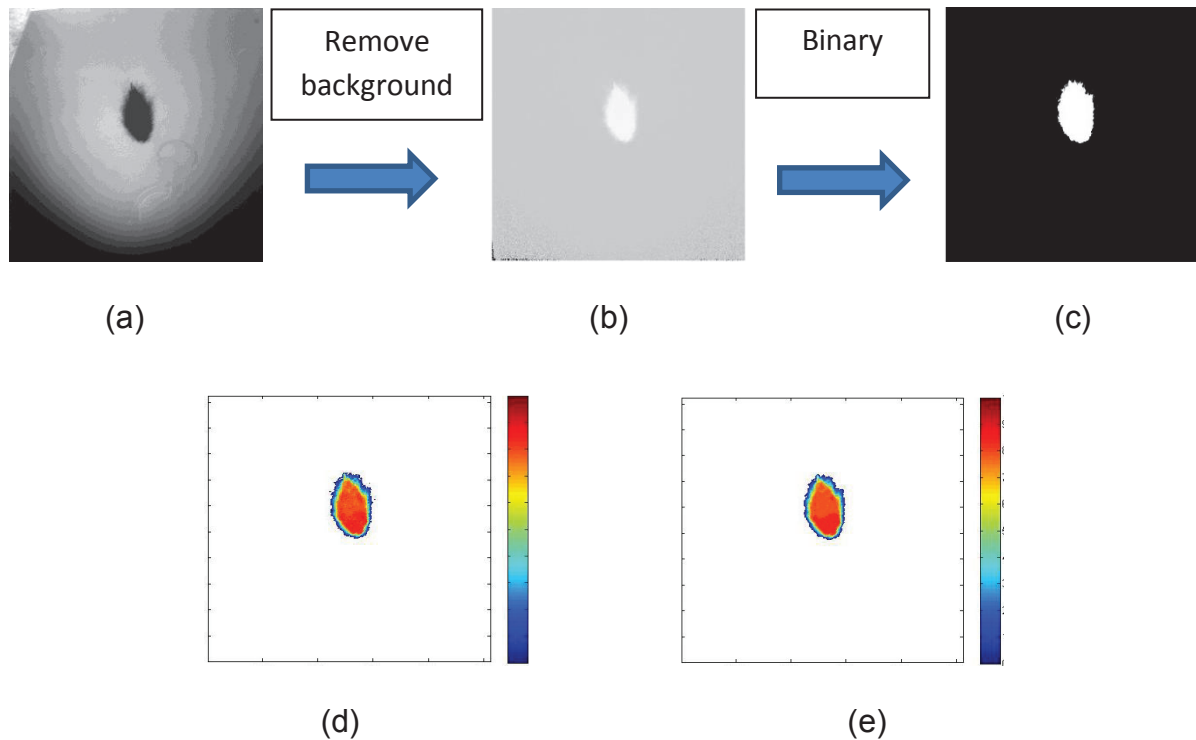


Figure 3.9 Image processing of the RIM images, (a) Raw image, (b) Background removed image, (c) Binary image, (d) Time filtered image, and (e) Time and space filtered image.

3.1.3 Numerical Simulation Setup of Spray and Wall Impingement

Spray Model

Simulations of multi-hole spray and impingement were carried out using CONVERGE [13], commercial three dimensional CFD software. The spray droplets undergo a number of subroutines: breakup, collision, vaporization and drop drag. If the fuel spray impacts the piston, the formation and evaporation of liquid fuel films should be considered. Among these physical processes, the breakup process is

critical to predict droplet velocity and size. In this study, the solid-cone spray characteristics were simulated using the Kelvin-Helmholtz/Rayleigh-Taylor (KH-RT) breakup model as shown in Figure 3.10. The KH model simulated the primary aerodynamic instability breakup, and the RT model calculated the secondary breakup due to decelerative instabilities. For the KH-RT breakup model, the breakup length was written as

$$L_b = C_{bl} \sqrt{\frac{\rho_l}{\rho_g}} d_0 \quad \text{Equation 3.5}$$

where ρ_l and ρ_g are the density of the fuel liquid and the ambient gas; d_0 is the diameter of the orifice; C_{bl} is the breakup length constant. Only KH instabilities are responsible for drop breakup inside of the breakup length, while both KH and RT mechanisms are activated beyond the breakup length.

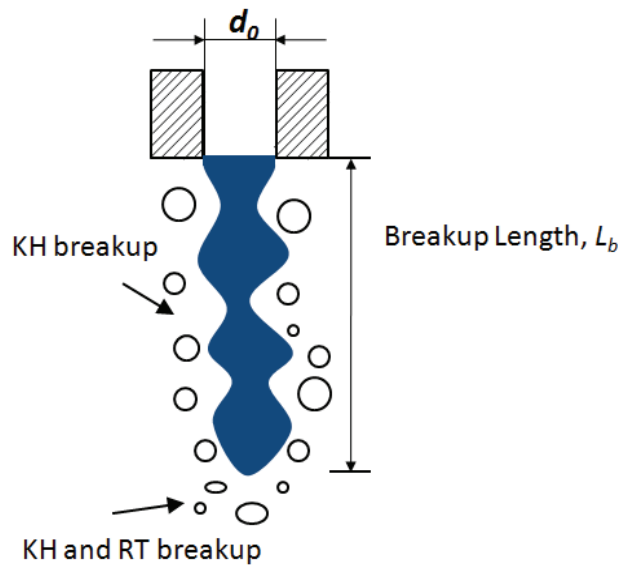


Figure 3.10 KH-RT breakup model.

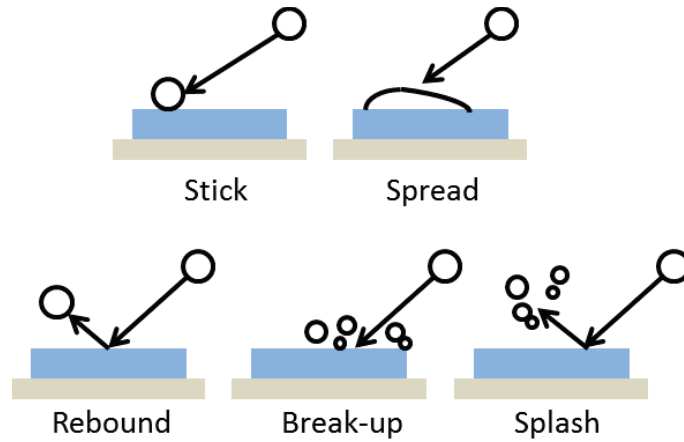


Figure 3.11 Collision regimes of spray wall interaction used in Converge

Wall film

Generally, the collision between an impinging drop and a wet surface may result in five different regimes: sticking, spreading, rebounding, breakup and splash as shown in Figure 3.11 [14]. The interaction of liquid drips and solid surfaces is modeled using a wall film model, which is a hybrid model that assumes individual particle-based quantities and film-based quantities [15]. The liquid film transport is modeled by the film momentum equation. The drop Weber number is defined as

$$We = \frac{\rho_l V_n^2 d}{\sigma} \quad \text{Equation 3.6}$$

where ρ_l is the liquid density, V_n is the drop velocity component normal to the surface, d is the drop diameter, and σ is the liquid surface tension. The criterion for splash is given by:

$$E^2 = \frac{We}{\min\left(\frac{h}{d}, 1\right) + \frac{\delta}{d}} > E_{\text{criterion}}^2 \quad \text{Equation 3.7}$$

where h is the local film thickness and δ is the boundary layer thickness calculated from the drop diameter and the Reynolds number.

The computational domain was a cylinder of Φ 150mm x180mm, which represented a constant volume vessel. The number of cells was in the range of 50,000 and 100,000, and the cell size was as follows: 2mm for the central region, 1mm for the each nozzle direction area, and 8mm for the other area. In addition to the embedded grid control, CONVERGE is able to use Adaptive Mesh Refinement (AMR) automatically to enhance the mesh around the spray edge. The level of embedding for velocity, temperature, and mass fraction in this study was set to 3, which made the mesh size 1mm when AMR was turned on. The maximum number of droplet parcels ensures the precise resolution of relevant droplet processes.

Simulation of wall film was also carried out using Ansys Fluent 15.0 [16]. In the simulation, conjugate heat transfer (CHT, with glass plate, 2mm thick), Eulerian Wall Film (EWF, Second-Order Implicit Method), and Local mesh adaption were adapted. In EWF model, the effects of sticking, rebounding, splashing and stripping were taken into account as shown in Figure 3.12.

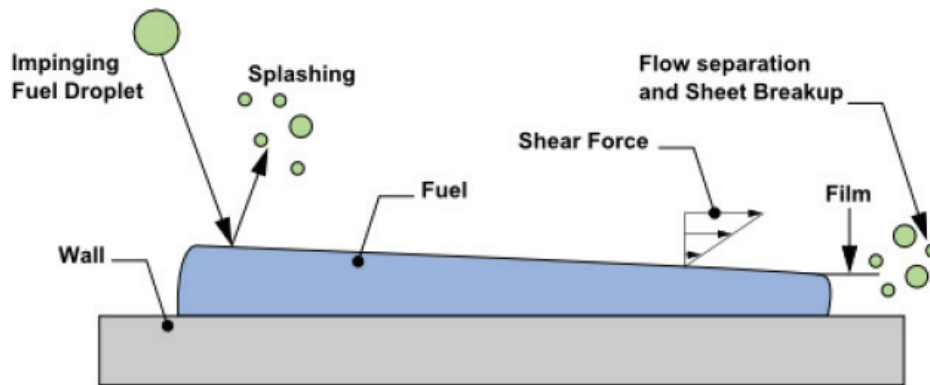


Figure 3.12 Collision regimes of spray wall interaction used in Fluent

CHAPTER 4 RESULTS AND DISCUSSION

This chapter presents results of the experiments and simulations for spray and wall film in the constant-volume chamber. The first section discusses the simulation and experimental results of the spray. The second section summarizes the fuel film results obtained from both the experiments and the simulation.

4.1 Spray and Wall Impingement

Spray vaporization was tested using the Schlieren visualization [17] [18] method under four different conditions as listed in Table 4.1, and the simulation under the same conditions was carried out using Converge as well.

Table 4.1 Test conditions for spray vaporization

	Air Temperature T_{air} [C]	Air Pressure P_{air} [bar]	Injection Temperature T_{inj} [C]	Injection Pressure P_{inj} [bar]	Injection Duration [ms]
Case1	50	1	55	70	1
Case2	50	2	55	70	1
Case3	50	1	55	100	1
Case4	50	2	55	100	1

The flow rate of the injection was first measured with a Bosch injection rate meter as shown in Figure 4.1. The injector is connected to a long tube; a pressure transducer and a temperature sensor are used to measure the transient pressure and temperature in the tube after the injection. The injection rate can be obtained from the following equation.

$$\frac{dq}{dt} = \frac{A \cdot P}{a \cdot \rho} \quad \text{Equation 4.1}$$

Here, dq/dt is the flow rate, A is the cross-sectional area of the pipe, P is the instantaneous pressure, a is the acoustic speed in the fluid, and ρ is the density of the fluid.

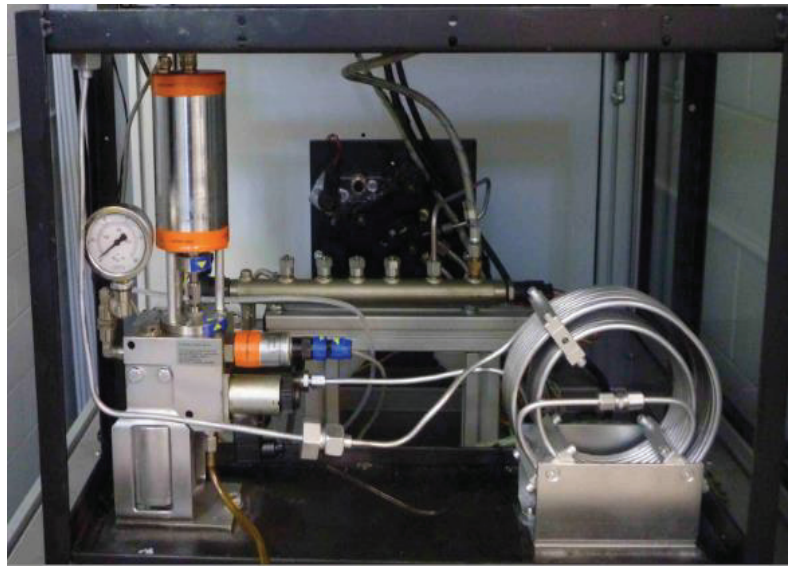
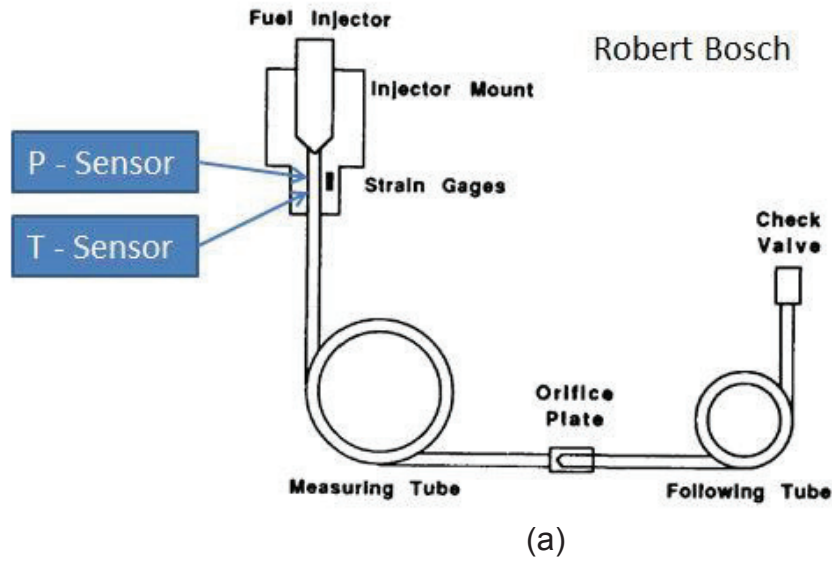


Figure 4.1 Schematic Figure (a) and apparatus photo (b) of injection rate meter

The experimental results for the injection rates under the injection pressure of 70bar and 100bar are shown in Figure 4.2, which will be further used in the simulation to set the flow rate shape.

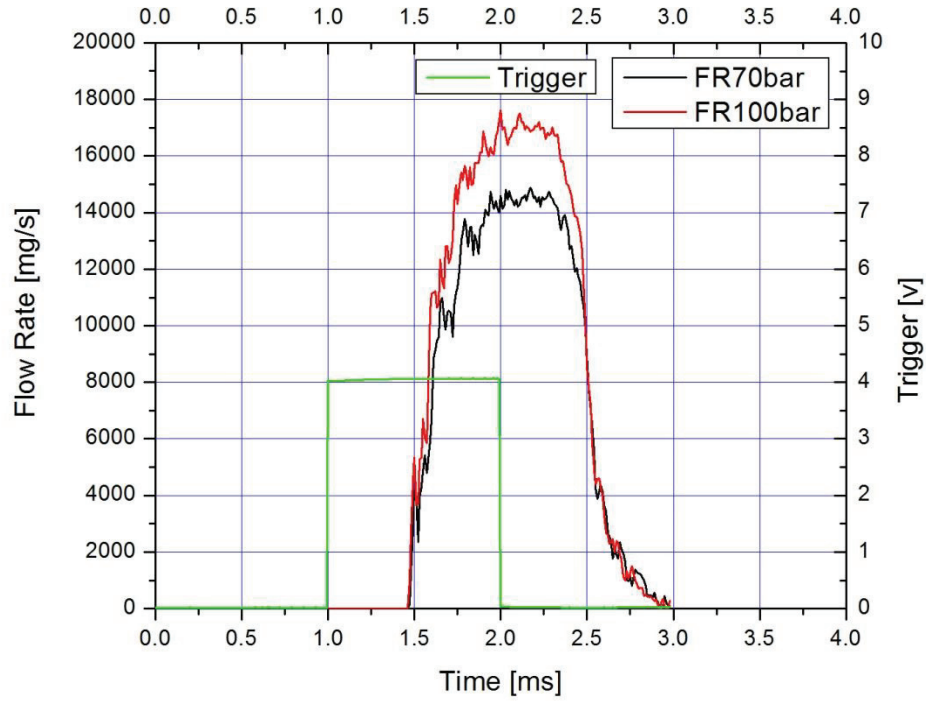
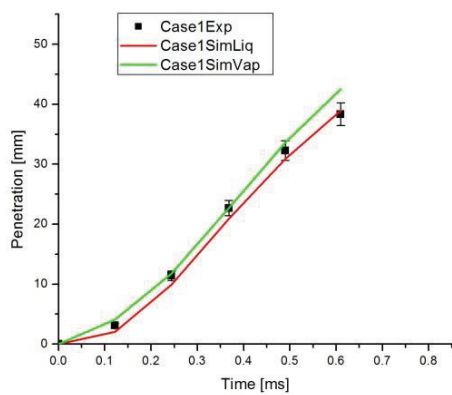
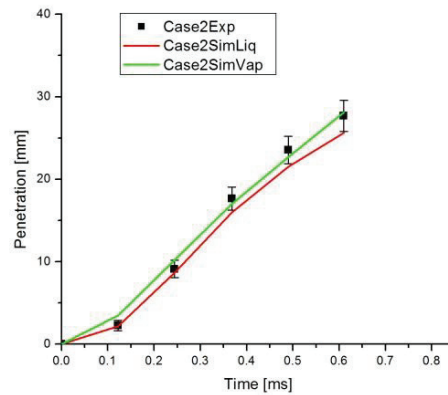


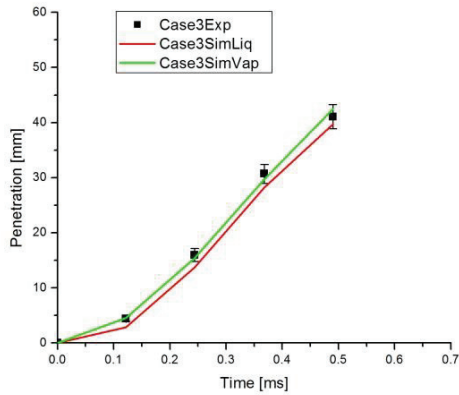
Figure 4.2 Injection rates under injection pressures of 70bar and 100bar



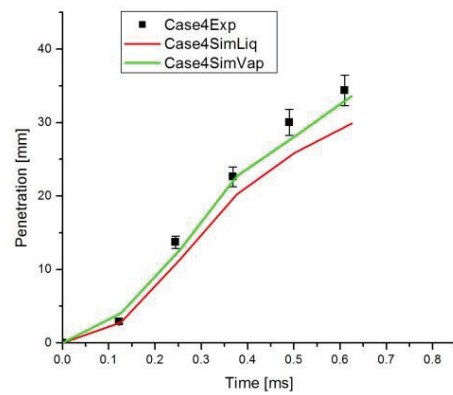
(a)



(b)



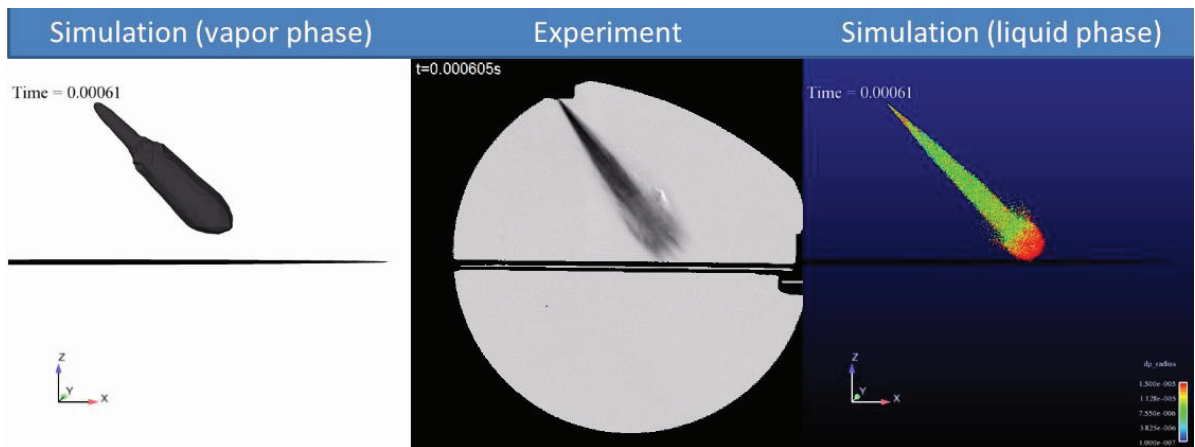
(c)



(d)

Figure 4.3 Experimental and CFD penetration of Case1(a), Case2(b), Case3(c) and Case4(d)

The penetration was first calculated based on the experimental results and compared with simulation data as shown in Figure 4.3. The black spots represent the experimental result; the green and red lines represent the simulated penetrations of vapor and liquid, respectively. It can be seen that the simulations agree well with the empirical data, especially at the early stage of injection. Higher injection pressure and lower chamber pressure will result in higher penetration.



(a)

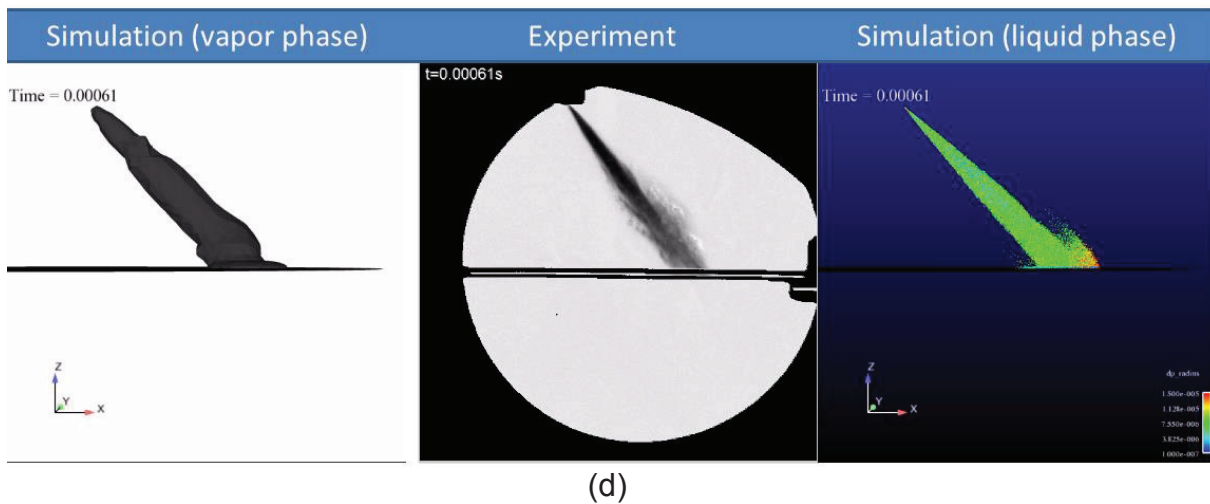
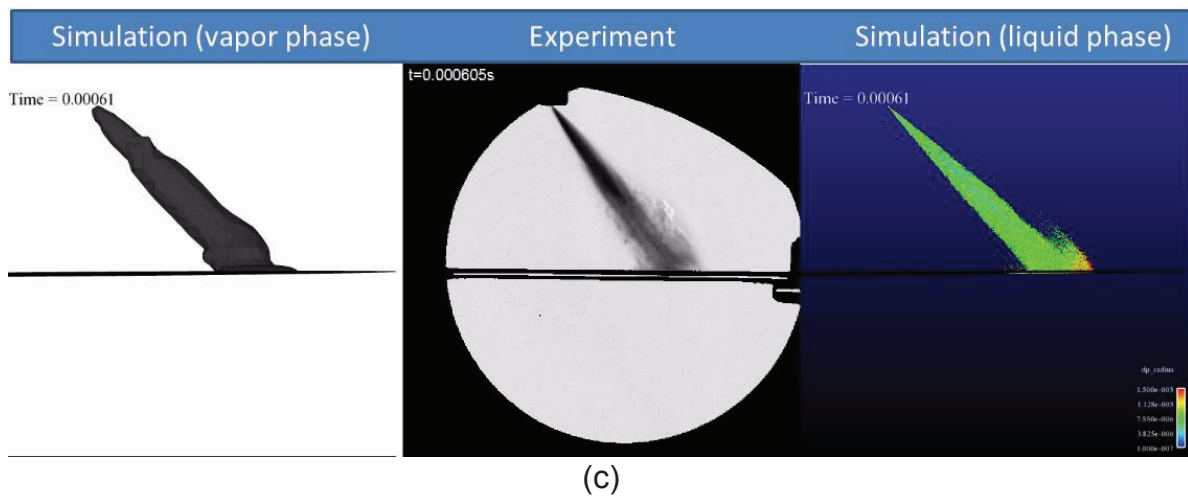
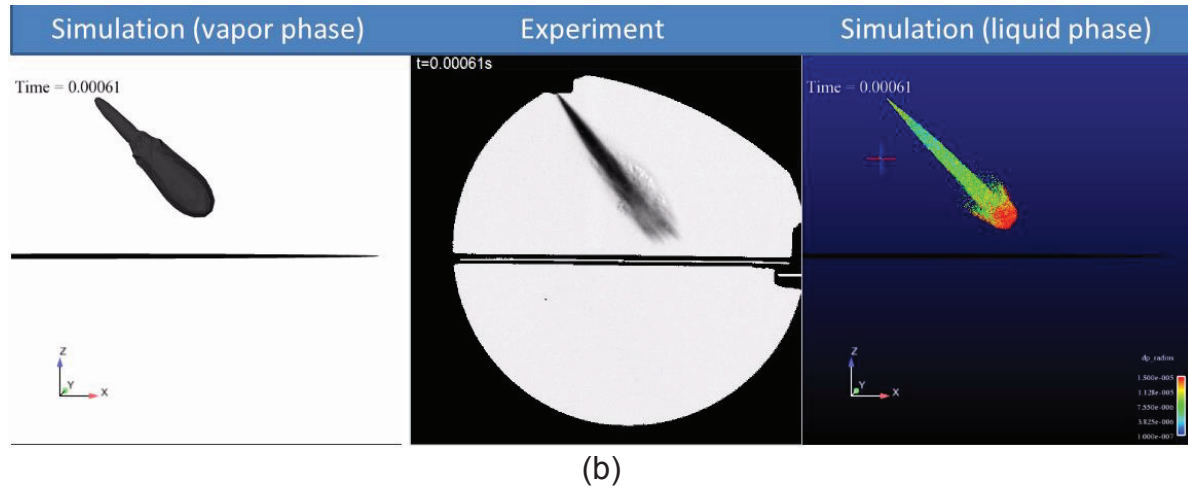


Figure 4.4 Spay Comparison between experimental and CFD results at 0.00061s after injection under $T_{air}=50C$, $P_{air}=1bar$, $T_{inj}=55C$, $P_{inj}=70bar$ (a), $T_{air}=50C$, $P_{air}=2bar$, $T_{inj}=55C$, $P_{inj}=70bar$ (b), $T_{air}=50C$, $P_{air}=1bar$, $T_{inj}=55C$, $P_{inj}=100bar$ (c), $T_{air}=50C$, $P_{air}=2bar$, $T_{inj}=55C$, $P_{inj}=100bar$ (d)

The comparison of overall spray shape between experimental and CFD results are shown in Figure 4.4, from which it can be seen that the agreements are very good. It can be indicated that better atomization and more evaporation can be obtained under lower air pressure and higher injection pressure.

4.2 Wall Impingement and RIM

Wall film was tested under different conditions as shown in Table 4.2.

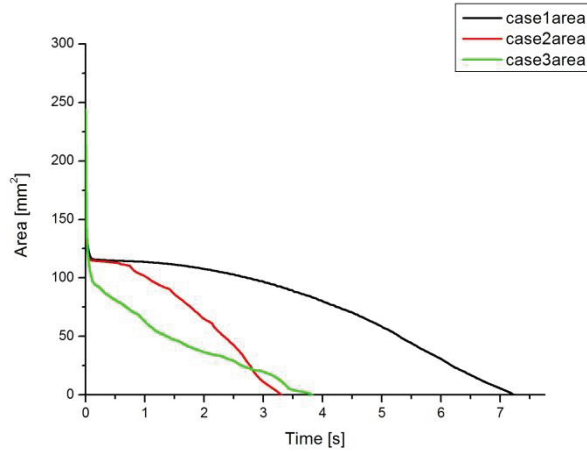
Table 4.2 Test matrix of wall film

	Test #	Injection angle* [°]	Distance [mm]	Air Temp [C]	Air Pres [bar]	Fuel Temp [C]	Fuel Pres [bar]	Pulse Width [ms]
Injection Angle Effect	1	30	30	50	2	55	100	1
	2	45	30	50	2	55	100	1
	3	60	30	50	2	55	100	1
Fuel Pressure Effect	4	60 /30	30	50	2	55	70	1
	5	60/30	30	50	2	55	140	1
Air Pressure Effect	6	60/30	30	50	1	55	70	1
	7	60/30	30	50	2	55	70	1
Air Temperature Effect	8	60/30	30	50	1	55	70	1
	9	60/30	30	75	1	55	70	1

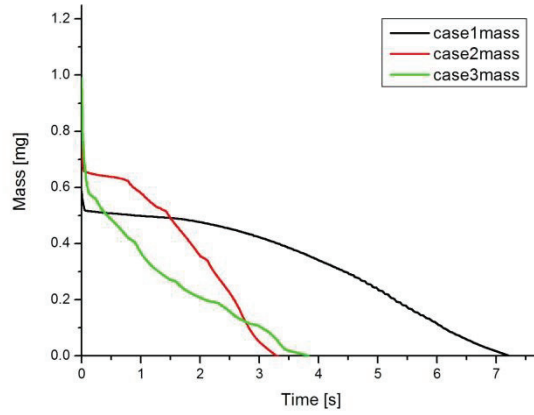
* The injection angle refers to the angle between the spray axis and the vertical direction.

4.2.1 Injection Angle Effect

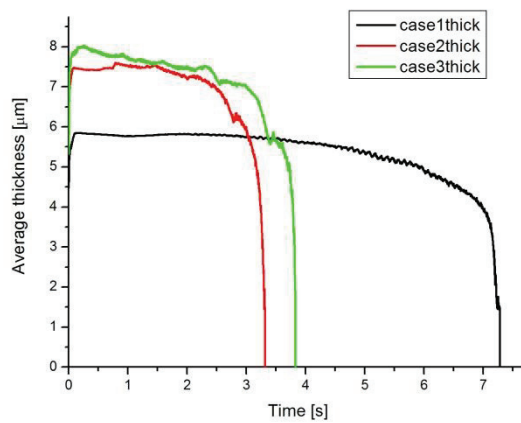
The effects of injection angle on wall film mass, area and average film thickness are shown in Figures 4.5 to 4.9. It can be indicated that a smaller injection angle leads to larger film mass and area, lower film thickness and longer evaporation duration. The reason may be that there are stronger impingement and rebound for spraying with smaller injection angles.



(a)

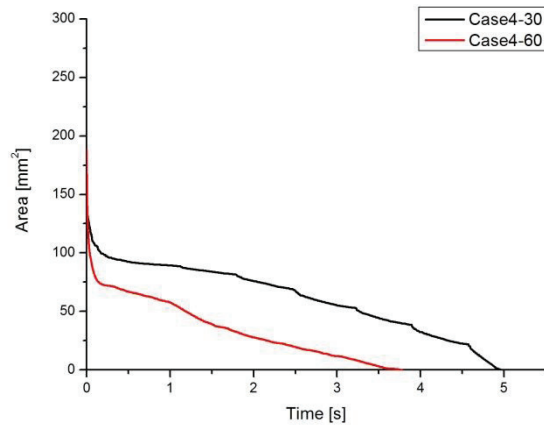


(b)

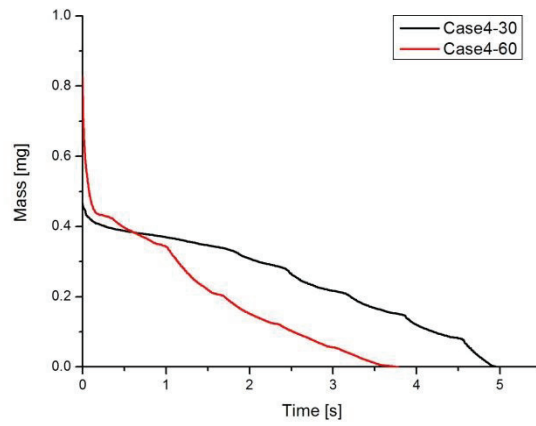


(c)

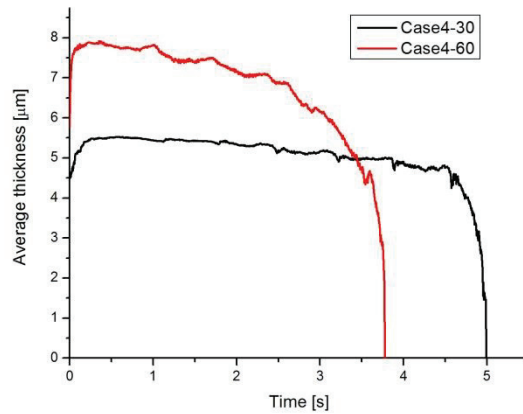
Figure 4.5 Wall films with different injection angles under $T_{\text{air}}=50\text{C}$, $P_{\text{air}}=2\text{bar}$, $T_{\text{fuel}}=55\text{C}$, $P_{\text{fuel}}=100\text{bar}$, total area (a), total mass (b), average thickness (c)



(a)

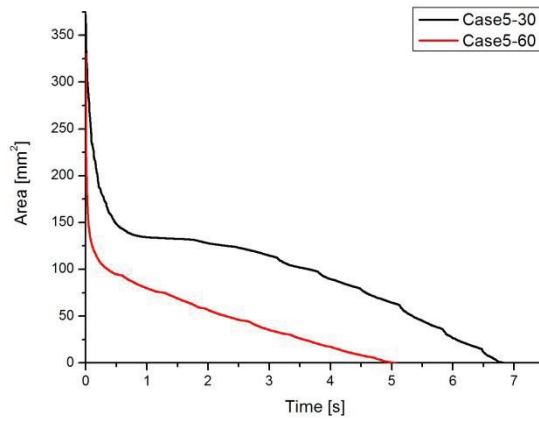


(b)

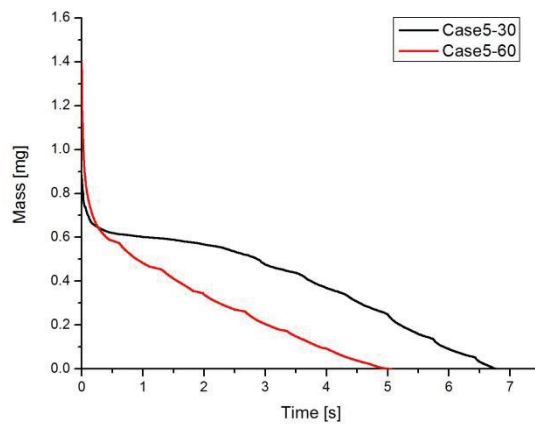


(c)

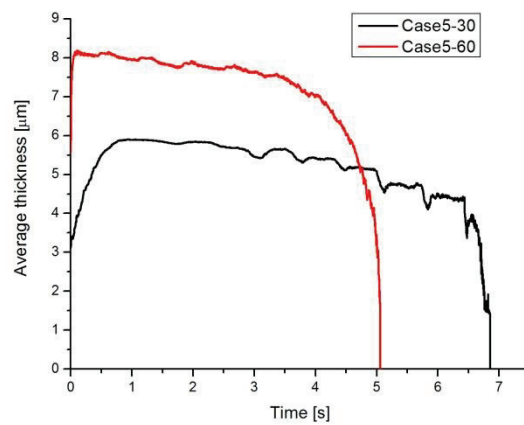
Figure 4.6 Wall films with different injection angles under $T_{\text{air}}=50\text{C}$, $P_{\text{air}}=2\text{bar}$, $T_{\text{fuel}}=55\text{C}$, $P_{\text{fuel}}=70\text{bar}$, total area (a), total mass (b), average thickness (c)



(a)

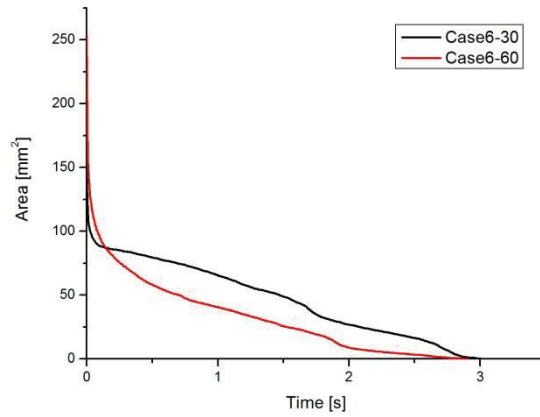


(b)

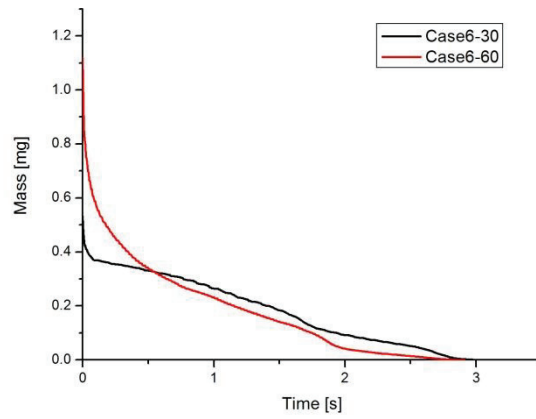


(c)

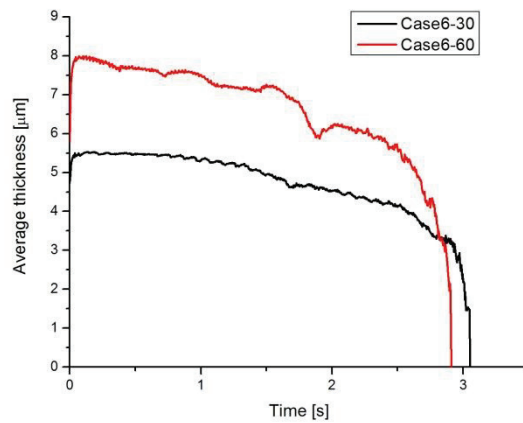
Figure 4.7 Wall films with different injection angles under $T_{\text{air}}=50\text{C}$, $P_{\text{air}}=2\text{bar}$, $T_{\text{fuel}}=55\text{C}$, $P_{\text{fuel}}=140\text{bar}$, total area (a), total mass (b), average thickness (c)



(a)

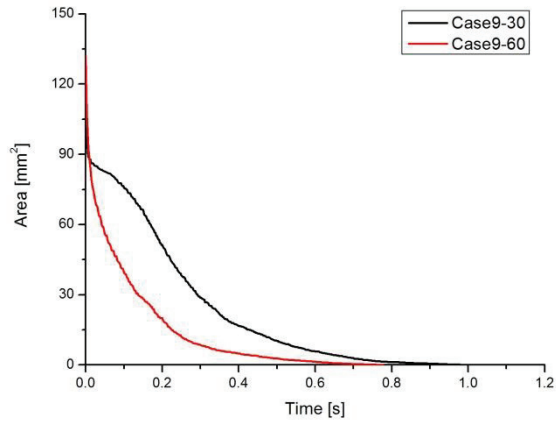


(b)

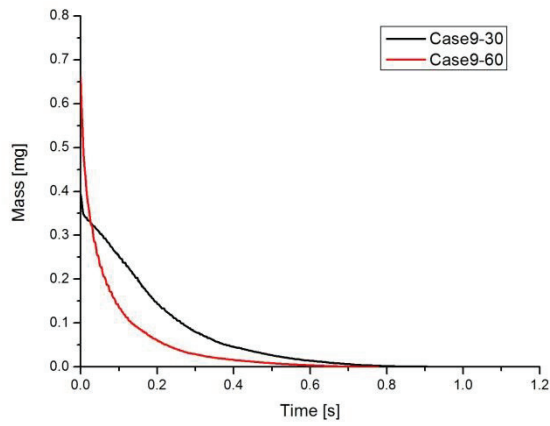


(c)

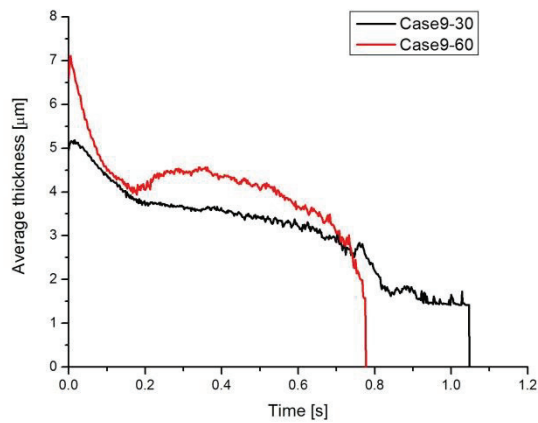
Figure 4.8 Wall films with different injection angles under $T_{\text{air}}=50\text{C}$, $P_{\text{air}}=1\text{bar}$, $T_{\text{fuel}}=55\text{C}$, $P_{\text{fuel}}=70\text{bar}$, total area (a), total mass (b), average thickness (c)



(a)



(b)

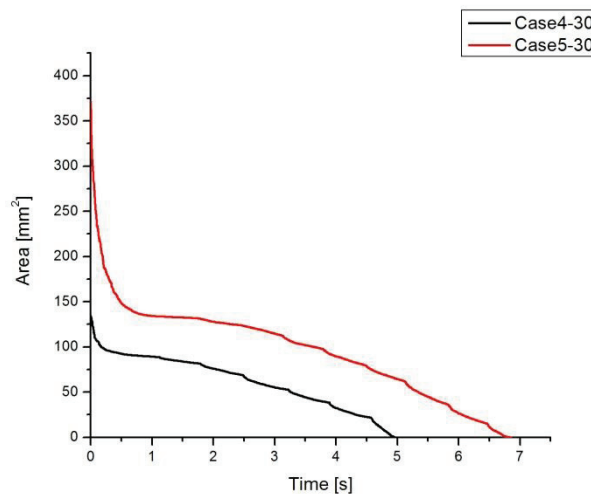


(c)

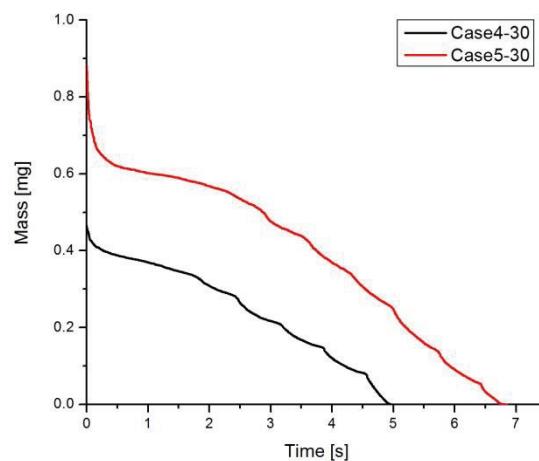
Figure 4.9 Wall films with different injection angles under $T_{\text{air}}=75\text{C}$, $P_{\text{air}}=1\text{bar}$, $T_{\text{fuel}}=55\text{C}$, $P_{\text{fuel}}=70\text{bar}$, total area (a), total mass (b), average thickness (c)

4.2.2 Fuel Pressure Effect

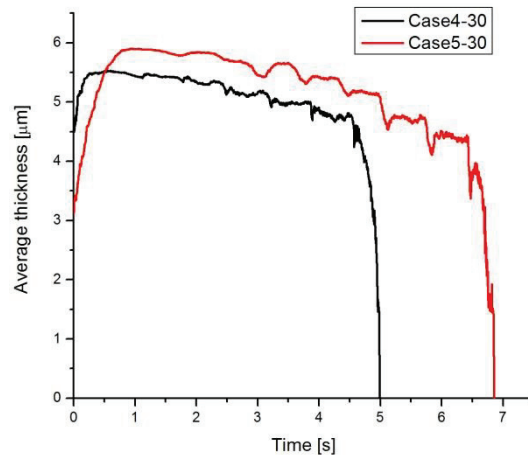
The effect of the fuel pressures of 70bar (case4) and 140bar (case5) on wall film is shown in Figure 4.10 and Figure 4.11. We can see that higher fuel pressure results in higher film mass, area, thickness, and evaporation duration. The reason is that more fuel is injected under higher fuel pressure, so more fuel deposits on the wall lead to higher mass, area, thickness and evaporation duration.



(a)

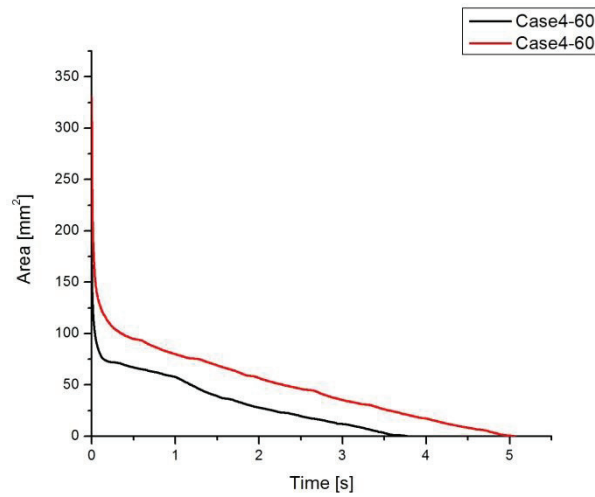


(b)

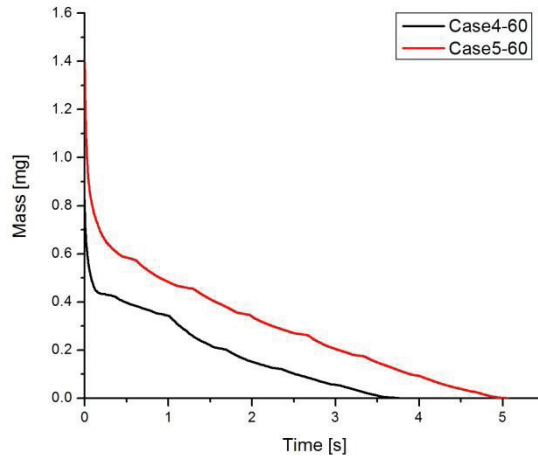


(c)

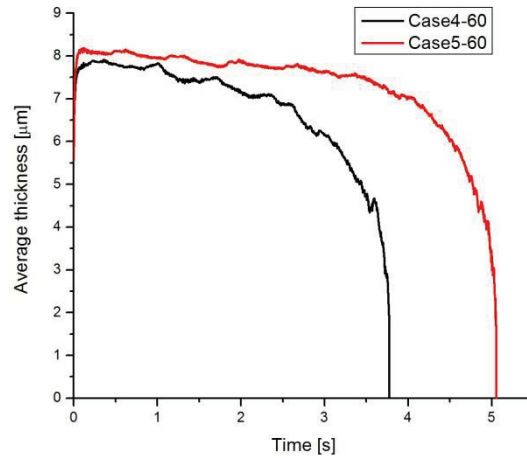
Figure 4.10 Wall films with P_{fuel} under $T_{air}=50C$, $P_{air}=2bar$, $T_{fuel}=55C$, $\theta_{inj}=30^\circ$, total area (a), total mass (b), average thickness (c)



(a)



(b)



(c)

Figure 4.11 Wall films with different P_{fuel} under $T_{\text{air}}=50\text{C}$, $P_{\text{air}}=2\text{bar}$, $T_{\text{fuel}}=55\text{C}$, $\theta_{\text{inj}}=60^\circ$, total area (a), total mass (b), average thickness (c)

4.2.3 Air Pressure Effect

The wall film was measured under different air pressures of 1bar (case6) and 2bar (case7). The results are shown in Figure 4.12 and Figure 4.13. It can be indicated that more fuel deposits on the wall under higher air pressure and

evaporates more slowly because fuel evaporates more slowly under higher ambient pressure.

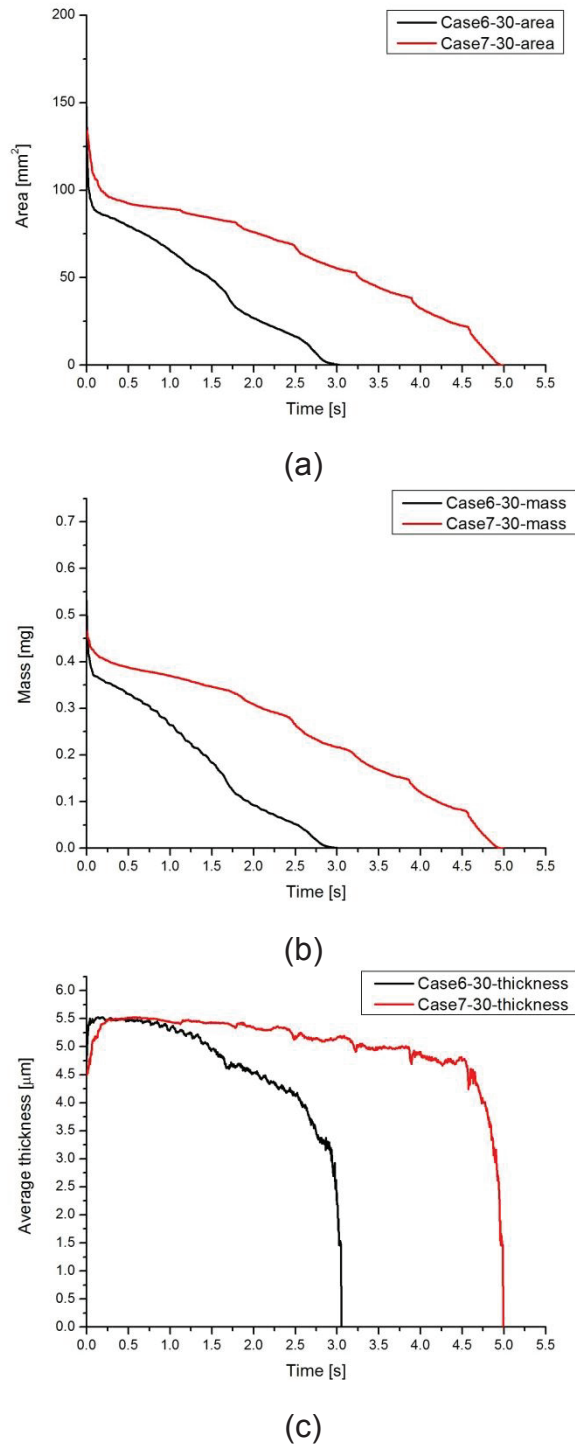
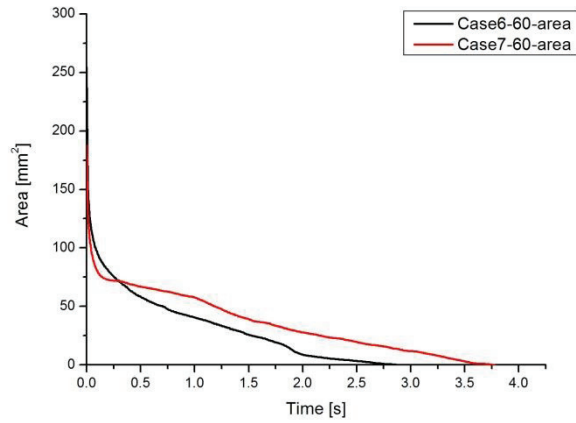
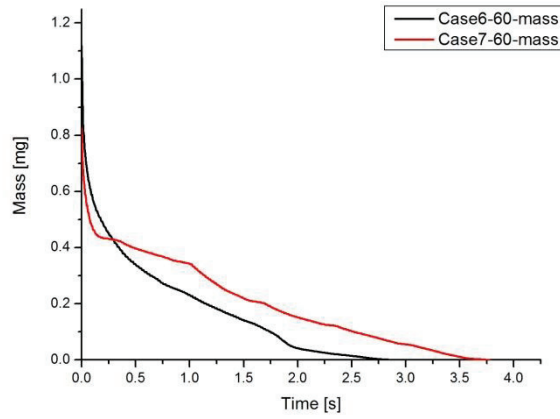


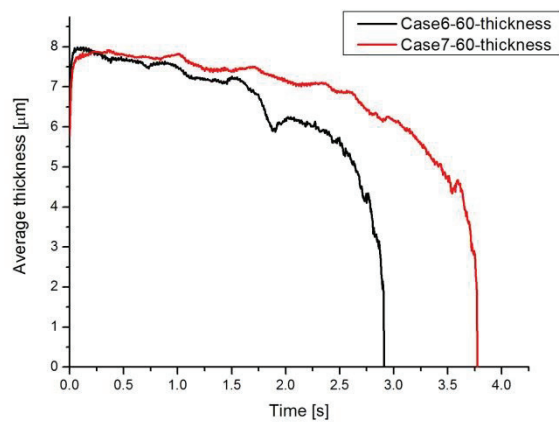
Figure 4.12 Wall films with different P_{air} under $T_{air}=50C$, $T_{fuel}=55C$, $P_{fuel}=70bar$, $\theta_{inj}=30^\circ$, total area (a), total mass (b), average thickness (c)



(a)



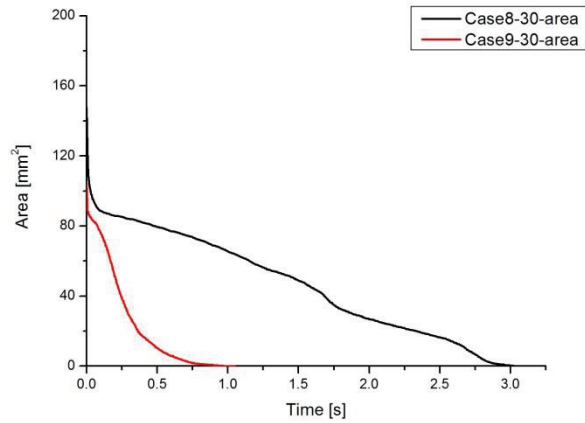
(b)



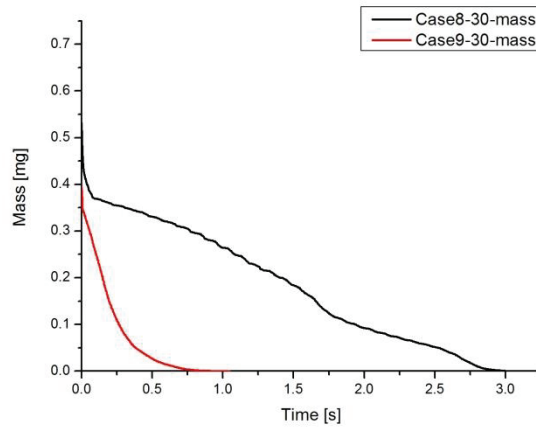
(c)

Figure 4.13 Wall films with different P_{air} under $T_{air}=50C$, $T_{fuel}=55C$, $P_{fuel}=70bar$, $\theta_{inj}=60^\circ$, total area (a), total mass (b), average thickness (c)

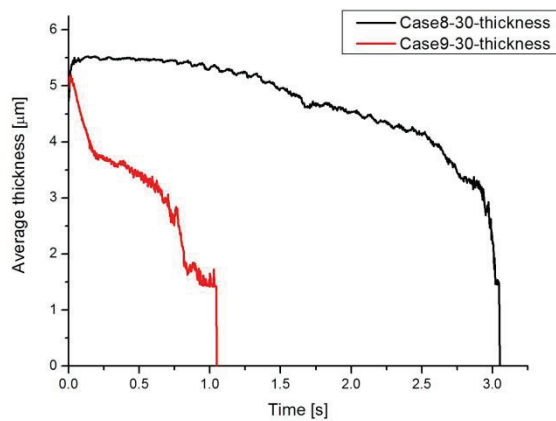
4.2.4 Air Temperature Effect



(a)

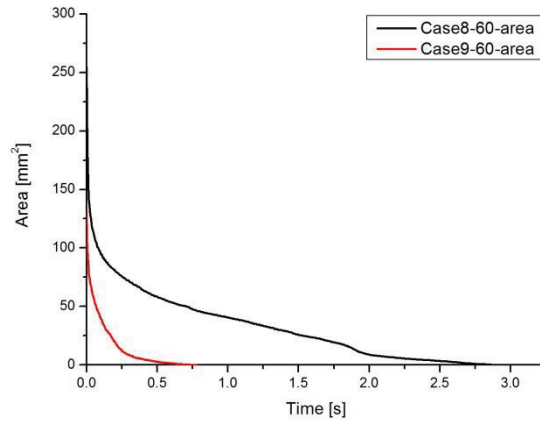


(b)

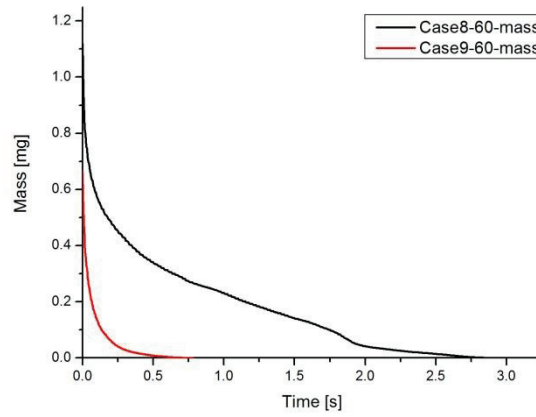


(c)

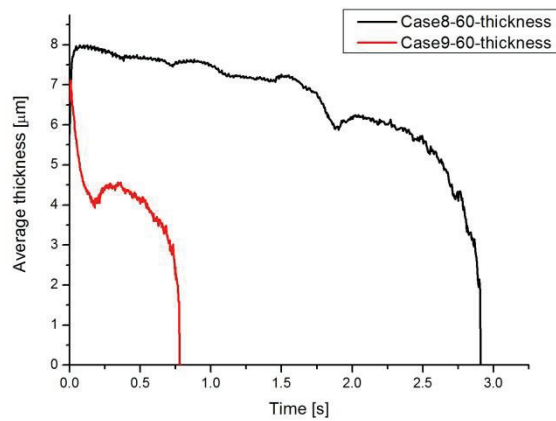
Figure 4.14 Wall films with different T_{air} under $P_{air}=1\text{bar}$, $T_{fuel}=55\text{C}$, $P_{fuel}=70\text{bar}$, $\theta_{inj}=30^\circ$, total area (a), total mass (b), average thickness (c)



(a)



(b)



(c)

Figure 4.15 Wall films with different T_{air} under $P_{\text{air}}=1\text{bar}$, $T_{\text{fuel}}=55\text{C}$, $P_{\text{fuel}}=70\text{bar}$, $\theta_{\text{inj}}=60^\circ$, total area (a), total mass (b), average thickness (c)

The wall film was measured under different air temperatures of 50C (case8) and 75C (case8). The results are shown in Figure 4.14 and Figure 4.15. It can be indicated that wall film is very sensitive to ambient temperature, and the fuel film evaporates much more quickly under higher ambient temperature due to the stronger heat transfer.

4.2.5 Simulation Results of Wall film

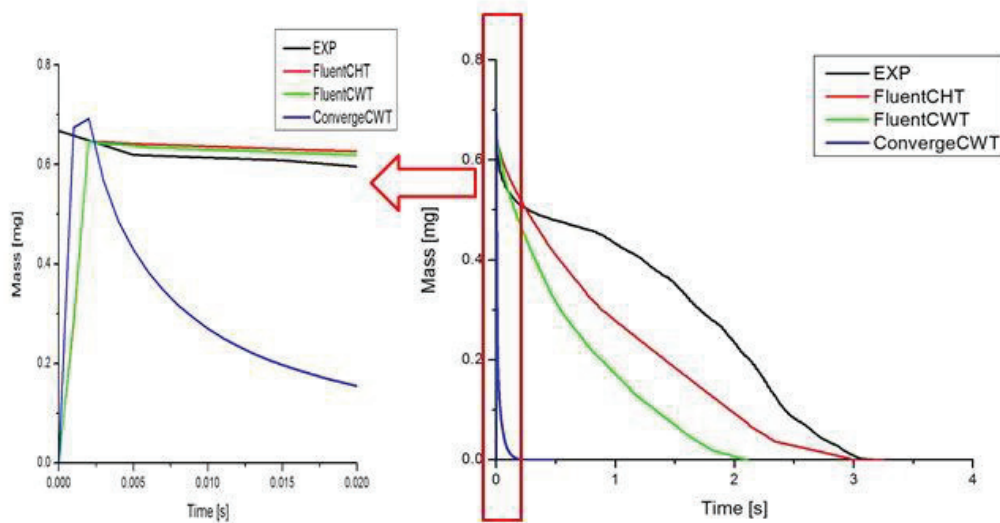
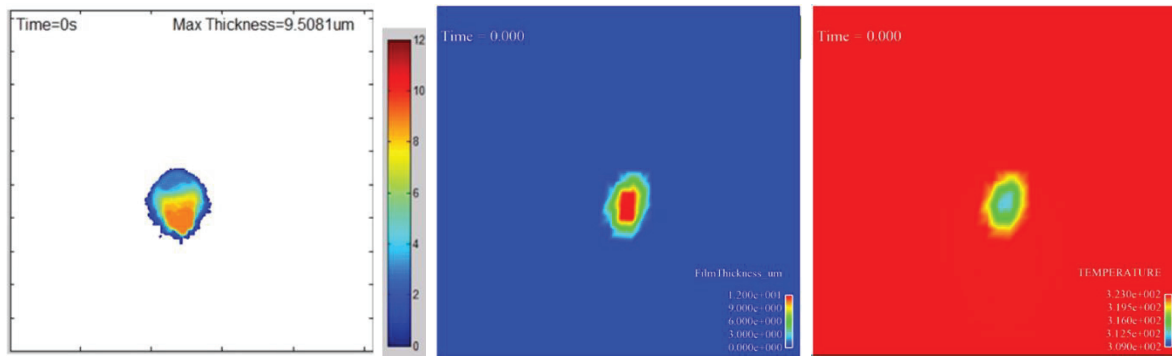


Figure 4.16 Comparison between experimental and CFD results of wall film under $T_{air}=50C$, $P_{air}=1bar$, $T_{fuel}=55C$, $P_{fuel}=70bar$

Simulations of the wall film were performed using commercial CFD code Converge and Fluent under the condition of $T_{air}=50C$, $P_{air}=1bar$, $T_{fuel}=55C$, $P_{fuel}=70bar$, and the results are shown in Figure 4.16. In the simulations, the rebound coefficient was adjusted to match the initial mass of the wall film as shown in Figure 4.16. In the simulation using Converge, constant wall temperature (CWT) model was used due to the limitation of the software, and both constant wall

temperature (CWT) model and conjugate heat transfer (CHT) model were used in the simulation using Fluent. It can be seen that the fuel film evaporates more quickly with the CWT model. The reason is that CWT model overestimates the wall temperature and leads to stronger heat transfer and fuel evaporation. However, the simulated evaporation obtained by Converge is even faster than that obtained by Fluent. The reason may depend on the break up model of Converge, which means the liquid particles are too small and evaporate more quickly. The simulated result using the CHT model matches more closely with the experimental result, and the spatial distribution of film thickness and temperature are shown in Figure 4.17. It can be seen that the simulated film thickness is close to the experimental results. The maximum temperature drop of the wall is 14C, which is very close to the reference value of 16C [19].



(a) (b) (c)
 Figure 4.17 Comparison of experimental spatial wall film thickness (a), simulated spatial wall film thickness (b) and spatial wall film temperature (c).

CHAPTER 5 CONCLUSION

5.1 Summary of the Work

In this work experimental and computational investigation was carried out for the spray vaporization and wall film of the single-hole injector. The Refractive Index Matching technique was used to measure the fuel film in a conditioned pressure chamber, and Converge and Fluent were used in the simulation. The conclusion is as follows:

1. Higher injection angle leads to higher film thickness but shorter evaporation duration.
2. Higher fuel pressure and air pressure will results in more fuel deposits on the wall and evaporates slower.
3. Fuel film is affected by the ambient temperature significantly and evaporates much faster under higher ambient temperature.
4. In the simulation, conjugate heat transfer (CHT) effect cannot be ignored, and the maximum temperature drop is around 14C.

5.2 Recommendation and Future Work

The surface conditions and heat transfer of the wall in RIM measurement and simulation should be considered for further study. The saturation of the scattering light in the RIM technique should be studied more carefully and avoided to improve the precision of the measurements.

REFERENCES

- [1] U.S. Environmental Protection Agency, National Emission Inventory Air Pollutant Emission Trends Web site www.epa.gov/ttn/chief/trends. (Additional resources: www.epa.gov/ttn/chief)
- [2] Zhao, F.-Q., Harrington, D. L., and Lai, M.-C., Automotive Gasoline Direct Injection Engines, Pittsburgh: Society of Automotive Engineers, 2002, R-315.
- [3] http://en.wikipedia.org/wiki/Ford_EcoBoost_engine. Accessed May 04, 2013.
- [4] Moreira, A.L.N., Moita, A.S., and Panao, M.R. Progress in Energy Combustion Science. 2010, 36: 544-580
- [5] Drake, M., Fansler, D., and Rosalik, M.E. Quantitative high-speed imaging of piston fuel films in direct-injection engines using a refractive-index-matching technique, 15th Annual Conference on Liquid Atomization and Spray Systems, Madison,WI, May 2002
- [6] Drake, M., Fansler, D., Solomon, A.S., and Rosalik, M.E. Piston Fuel Films as a Source of Smoke and Hydrocarbon Emissions from a Wall-Controlled Spark-Ignited Direct-Injection Engine, SAE Technical Paper 2003-01-0547, 2003
- [7] Yang, B., Ghandhi, J. Measurement of Diesel Spray Impingement and Fuel Film Characteristics Using Refractive Index Matching Method, SAE Technical Paper 2007-01-0485, 2007
- [8] Zheng, Y., Xie, X., et al., Measurement and Simulation of DI Spray Impingements and Film Characteristics, 12th Triennial International Conference on Liquid Atomization and Spray Systems, Heidelberg, Germany, September, 2012

- [9] Lindgren, R., and Denbratt, I., Influence of Wall Properties on the Characteristics of a Gasoline Spray after Wall Impingement, SAE Technical Paper 2004-01-1951, 2004.
- [10] Montorsi, L., Magnusson, A., and Andersson, S., Numerical and Experimental Analysis of the Wall Film Thickness for Diesel Fuel Sprays Impinging on a Temperature-Controlled Wall, SAE Technical Paper 2007-01-0486, 2007.
- [11] Montanaro, A., Malaguti, S., Alfuso, S., Wall Impingement Process of a Multi-Hole GDI Spray: Experimental and Numerical Investigation, SAE Technical Paper 2012-01-1266, 2012.
- [12] Rena, H., Xu, S., Wu, S., Effects of gravity on the shape of liquid droplets, Optics Communications, 2010, 283: 3255-3258
- [13] Richards, K. J., Senecal, P. K., and Pomraning, E., CONVERGE (Version 2.0.0), Convergent Science, Inc., Middleton, WI (2013).
- [14] Donald W. S., Christopher J. R., Multi-dimensional modeling of thin liquid films and spray-wall interactions resulting from impinging sprays, International Journal of Heat and Mass Transfer, 1998, 41: Pages 3037–3054
- [15] Schmidt, D. P., Nouar, I., Senecal, P. K., Hoffman, J., Rutland, C. J., Martin, J., and Reitz, R. D., Pressure-Swirl Atomization in the Near Field. SAE Technical Paper 1999-01-0496.
- [16] Ansys Fluent, Ansys Inc, Products 15.0, 2014
- [17] Joh, M., Huh K. Y., Yoo, J.-H., and Lai, M.-C. Numerical Prediction and Validation of Fuel Spray Behavior in a Gasoline Direct-Injection Engine [J]. J. Fuels & Lubricants, 2002, 110(4): 2387-2404.

- [18] Schmitz, I., Ipp, W., and Leipertz, A., Flash Boiling Effects on the Development of Gasoline Direct Injection Sprays [J]. SAE 2002-01-2661, 2002.
- [19] Schulz, F., Schmidt, J., Infrared thermography based fuel film investigations, 12th Triennial International Conference on Liquid Atomization and Spray Systems, Heidelberg, Germany, September, 2012

ABSTRACT**SIMULATIONS AND MEASUREMENTS OF FUEL FILM USING REFRACTIVE INDEX MATCHING METHOD**

by

FENGKUN WANG**MAY 2014****Advisor:** Dr. Ming-Chia Lai**Major:** Mechanical Engineering**Degree:** Master of Science

Direct Injection (DI) has been known for its improved performance and efficiency in gasoline spark-ignition engines. However, wall wetting is inevitable and the source of UHC and PM. In order to take advantage of the GDI technology, it is important to investigate spray wall interactions in detail.

Numerical and experimental studies are carried out for spray and wall impingements in an optical constant volume vessel. The fuel film was measured spatially and temporally using the Refractive Index Matching (RIM) technique. Based on the experimental results, the effects of injection angle, injection pressure, air pressure, and air temperature on wall film were evaluated quantitatively.

The CFD simulation with selected models of spray was first validated using the experimental measurements of spray visualization, and very good agreement in penetration and overall spray shape were achieved. For the wall film, the conjugate heat transfer model (CHT) was employed using Fluent, and fair agreement was obtained.

AUTOBIOGRAPHICAL STATEMENT

Fengkun Wang obtained his bachelor degree in mechanical engineering from Xi'an Jiaotong University in China and joined Wayne State University in January 2013 as a master candidate in mechanical engineering. His research interest includes spray and wall impingement, gasoline/diesel injector analysis, fuel air mixing and combustion diagnostics and simulation.